AD
AD-E404 224

Technical Report ARMET-TR-18079

INFINITE CYLINDER MODEL FOR MAGNETOMETERS ON PROJECTILES

Aaron Barton

August 2020

U.S. ARMY COMBAT CAPABILITIES DEVELOPMENT
COMMAND ARMAMENTS CENTER

Munitions Engineering Technology Center

Picatinny Arsenal, New Jersey

REPORT DOCUMENTATION PAGE	*Form Approved* *OMB No. 0704-01-0188*

1. REPORT DATE (DD-MM-YYYY) August 2020	2. REPORT TYPE Final	3. DATES COVERED (*From - To*) May 2016 – June 2018

4. TITLE AND SUBTITLE Infinite Cylinder Model for Magnetometers on Projectiles	5a. CONTRACT NUMBER
	5b. GRANT NUMBER
	5c. PROGRAM ELEMENT NUMBER
6. AUTHORS Aaron Barton	5d. PROJECT NUMBER
	5e. TASK NUMBER
	5f. WORK UNIT NUMBER

7. PERFORMING ORGANIZATION NAME(S) AND ADDRESS(ES) U.S. Army CCDC AC, METC Fuze & Precision Armaments Directorate (FCDD-ACM-FI) Picatinny Arsenal, NJ 07806-5000	8. PERFORMING ORGANIZATION REPORT NUMBER
9. SPONSORING/MONITORING AGENCY NAME(S) AND ADDRESS(ES) U.S. Army CCDC AC, ESIC Knowledge & Process Management Office (FCDD-ACE-K) Picatinny Arsenal, NJ 07806-5000	10. SPONSOR/MONITOR'S ACRONYM(S)
	11. SPONSOR/MONITOR'S REPORT NUMBER(S) Technical Report ARMET-TR-18079

12. DISTRIBUTION/AVAILABILITY STATEMENT
Approved for public release; distribution is unlimited.

13. SUPPLEMENTARY NOTES

14. ABSTRACT

A projectile body is modeled as a hollow thick shell infinite cylinder subject to a rotating transverse B-field, in order to study the effects of soft-iron and eddy-current distortion on the geomagnetic field as the projectile spins during flight to predict magnetometer reading error. An analytical two-dimensional (2D) model is derived using modified Bessel functions, which capture the effects of material permeability and conductivity on the field distortion. Two example cylinders are studied: aluminum and steel, each 155 mm in diameter. The derivation results show that induced magnetic dipole moments are formed on the exterior of the cylinders, while an attenuated and rotated uniform field is formed on the interior of the cylinders. The complex moments, attenuation factors, and rotation angles are plotted against spin rate. Variation with material temperature is explored. The results are compared against 2D finite element analysis simulations using ANSYS Electronics Desktop. A three-dimensional finite cylinder is also modeled to explore the effects of length against the validity of the 2D thick shell model. Methods of distortion correction are discussed, along with optimum placement of magnetometers.

15. SUBJECT TERMS

Telemetry Wireless High-g Gun launched DFuze Aerofuze Magnetometers
Precision guidance Geomagnetic field Eddy currents Compass Soft-iron Hard-iron
Permeability Thick shell model Thin shell model Magnetic diffusion

16. SECURITY CLASSIFICATION OF:			17. LIMITATION OF ABSTRACT	18. NUMBER OF PAGES	19a. NAME OF RESPONSIBLE PERSON Aaron E. Barton
a. REPORT U	b. ABSTRACT U	c. THIS PAGE U	SAR	59	19b. TELEPHONE NUMBER (Include area code)

Standard Form 298 (Rev. 8/98)
Prescribed by ANSI Std. Z39.18

CONTENTS

FIGURES

FIGURES
(continued)

ACKNOWLEDGMENTS

The author would like to thank Moshe Hamaoui of the U.S. Army Research Laboratory (ARL), Adelphi, MD, for reviewing drafts of this work and providing guidance; David Grasing of the U.S. Army Combat Capabilities Development Command Armaments Center (CCDC AC), Picatinny Arsenal, NJ, for reviewing the mathematical derivations; Christopher Stout of the CCDC AC for funding this work as a part of the Affordable Precision Technologies program; Tom Harkins of the ARL for discussions on historical magnetometer usage on munitions; and the ANSYS staff for their support in using their modelling and simulation tools.

INTRODUCTION

Magnetometers are used for smart projectile guidance and navigation as well as for projectile flight dynamic characterization, offering the potential to determine attitude and roll angle information using the Earth’s magnetic (geomagnetic) field as a reference vector. However, using a magnetometer on a projectile in flight is challenging, as the geomagnetic field near the magnetometer becomes distorted by the projectile body, especially in spin-stabilized projectiles. These distortions can be characterized into four groups: soft-iron, hard-iron, eddy-current, and electronic interferences.

Soft-iron distortions are caused by magnetic polarization of the iron-content of the projectile body, which forms in the direction of the geomagnetic field, creating an induced paramagnetic dipole. The nature of this distortion is to warp the locus of the points measured by a magnetometer from an origin-centered sphere into an ellipse. Hard-iron distortions are caused by permanent magnetization of the iron content of the projectile and are independent of the direction of the geomagnetic field. This can also vary between firings due to muzzle exit magnetization from ionized gun gases. The nature of this distortion is to shift the magnetometer locus points by an offset. Electronic interferences are caused by other electronics on the smart projectile that affect the magnetometer such as nearby current carrying wiring, stray magnetic fields from motors or generators, and radio frequency (RF) interference from wireless transmitters.

Eddy-current distortions occur when the geomagnetic field induces currents on the projectile metal body due to its spin and occur whether the metal is ferrous or not. These currents create two effects:

1. There is an induced diamagnetic dipole formed outside the body of the projectile, which acts to oppose the geomagnetic field.
2. The magnetic field on the outer surface of the projectile diffuses towards the center of the body.

The induced diamagnetic dipole forms in the opposite direction of the spinning geomagnetic field and has an amplitude and phase that varies with the frequency of spin and the conductivity and permeability of the metal. A magnetometer placed just outside of the projectile’s metal frame (such as under a radome) would measure the vector sum of the B-field created at that point by the induced diamagnetic dipole and the geomagnetic field. A magnetometer inside of the projectile’s metal frame would measure an attenuated and rotated field that results from the diffusion of the field on the surface, which varies with rate of spin, conductivity and permeability of the metal, temperature of the metal, and the thickness of the projectile sidewall. As the spin frequency increases, the center of the projectile becomes increasingly shielded from the geomagnetic field. These effects are displayed in figures 1 and 2, which show the results of a magnetic simulation of a 155 x 860-mm hollow cylinder in a rotating transverse B-field using ANSOFT Maxwell.

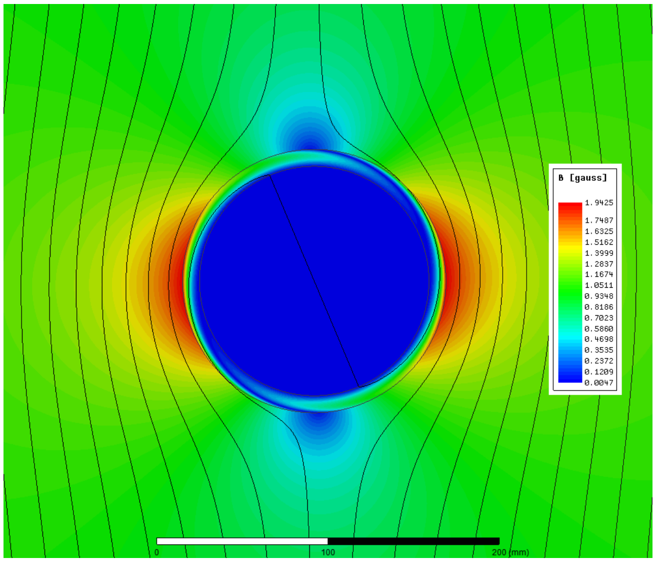

Note: B-field magnitude and flux lines shown. Cylinder dimensions: 155-mm outer diameter, 10-mm wall thickness, infinite length. Transverse field rotating at 300 Hz, shown at phase = 0 deg

Figure 1
Two-dimensional (2D) B-field simulation of infinite length aluminum cylinder in a rotating transverse field

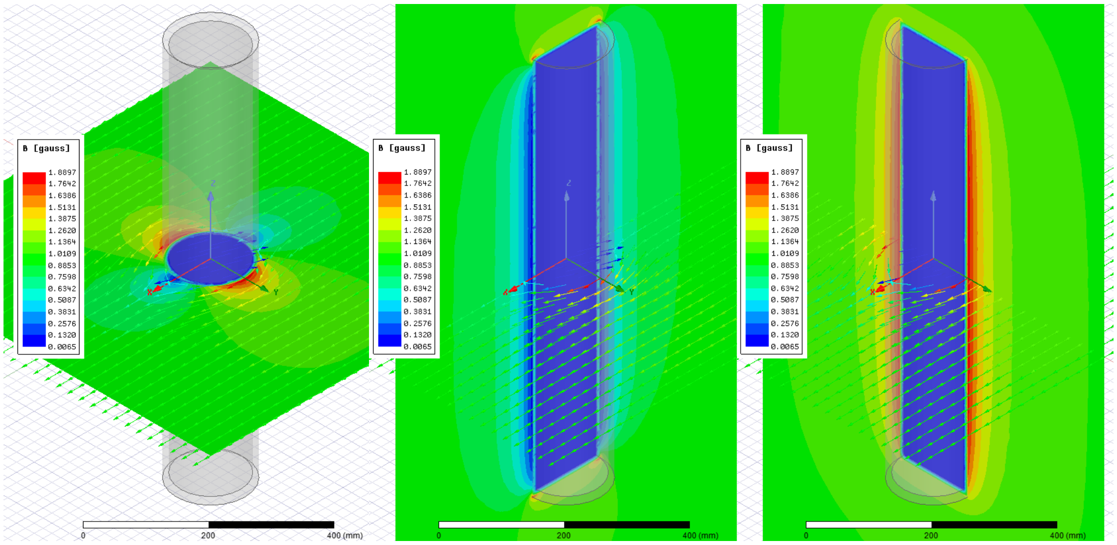

Note: B-field magnitude and vector plots shown. Cylinder dimensions: 155-mm outer diameter, 860-mm length, 10-mm wall thickness. Transverse field rotating at 300 Hz, shown at phase = 0 deg

Figure 2
Three-dimensional (3D) B-field simulation of a finite length aluminum cylinder in a transverse rotating field

Much work has been done observing the effects of these distortions on projectile-based magnetometers (refs. 1 and 2) and in developing algorithms to compensate for these distortions (refs. 3 and 4). The simplest method of correcting for magnetic deviation is to have a lookup table that offers a correction for the measurement. This assumes that the deviation can be measured over spin rate and temperature and is consistent between individual projectile rounds. Reference 4 discusses a state estimator, which contains three parameters: an attenuation factor, a distortion factor, and an axial factor. The focus of using modeling and simulation is to develop an understanding of these factors for different projectile and projectile fuze shapes and materials and to be able to predict them without having to perform extensive testing.

EDDY-CURRENT MODELING

In the reference frame of a spin-stabilized projectile, where the spin rate is greater than the pitching and yawing rates, the geomagnetic field will appear as a vector rotating in a cone around the spin axis, whose interior angle is referred to as σ_m. As shown in figure 3, this vector can be divided into the sum of two components: a slow varying axial field $\vec{B}_{axial}$, which points along the axis of rotation, and a rotating transverse field $\overrightarrow{B_t}$, which rotates in the plane of rotation. Calculating roll angle (such as for up-finding applications) relies on having an accurate, undistorted measurement of $\overrightarrow{B_t}$.

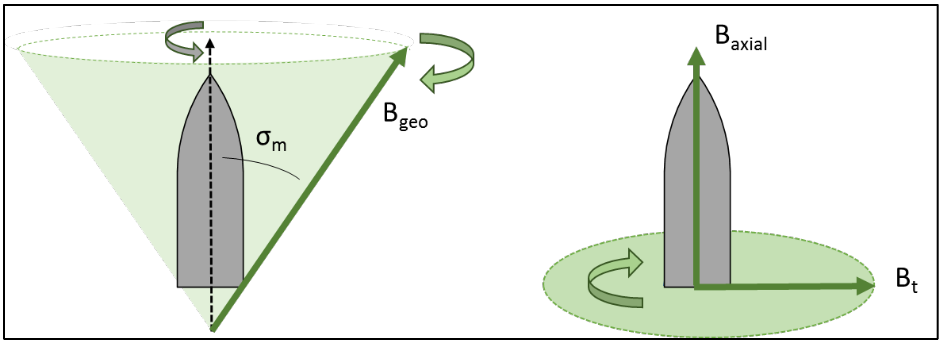

Figure 3
Diagram of geomagnetic field under spin

The transverse field $\overrightarrow{B_t}$ will be subject to eddy-current distortions by the projectile body. It is assumed that $\vec{B}_{axial}$ is slow varying enough that eddy-current distortions on it can be ignored. For a magnetometer placed midway in a projectile (such as within an inertial navigation unit), the cross section of the projectile can be treated as if it were a hollow cylinder of infinite extent. The infinite cylinder model can be used to understand the changes in direction and amplitude of $\overrightarrow{B_t}$. It will be seen in the thick-shell infinite cylinder model, and also the thin-shell infinite cylinder model given in appendix A, that an induced 2D dipole forms outside the shell. This has an amplitude and orientation that varies with the frequency of spin, conductivity, and permeability of the metal. As the spin rate becomes higher, or as the conductivity of the metal increases, this dipole becomes increasingly diamagnetic, acting to oppose the geomagnetic field and divert it around the shell. Inside the hollow free space section of the shell, it will be seen that there remains a uniform B-field much like the original geomagnetic field, only it is both attenuated in magnitude and shifted in orientation. As the spin-rate becomes higher, or as the conductivity of the metal increases, the magnitude of this field approaches zero.

This paper will provide analytical solutions for the B-field of a thick-shelled, infinitely-long conducting cylinder subject to a rotating uniform transverse B-field. The solutions involve solving for the magnetic vector potential $\vec{A}$ in polar coordinates, assuming a magneto-quasi-static system, in the Coulomb gauge and assuming no active sources or free electric charge. The governing equations for the

A-field become Laplace's equation (in the free space outside and inside the thin and thick shells) and the diffusion equation (for within the conducting portion of the thick shell). The latter is derived in appendix B from Maxwell's equations. The rotating B-field is first modelled as an oscillating uniform field directed along a single Cartesian axis and is treated as a boundary condition on the magnetic vector potential at infinity. The sum of two of these solutions, in phase-quadrature in space and time, is used to model a rotating field. Reference 5 is used heavily in these derivations. Plots are generated in MATLAB for several solved quantities, and the equations that were used are presented in boxes.

Two shell materials are used in this report: steel and aluminum. The former is ferrous and is treated as a material with linear permeability (it is assumed that the material has been sufficiently degaussed and that the geomagnetic field is not strong enough to change the material permeability away from its initial permeability); the latter is non-ferrous. Material properties that were used in developing plots and in finite element analysis (FEA) simulations are given in table 1.

Table 1
Material properties

Material	**Air**	**Steel**	**Aluminum**
Conductivity at 20°C (σ)	0	4.54e6 S/m	3.5e7 S/m
Resistivity temperature coefficient (α_r)	0	0.0024	0.0039
Permeability (μ)	μ_o =1.256e-6 H/m	83 * μ_o	1 * μ_o

Another model, referred to as the thin shell model and given in appendix A, is the case where the wall thickness of the cylinder is negligibly thin and is made of nonmagnetic material. The thin shell model is not generally valid for typical projectile sidewall widths. However, insight can be gained from studying it.

THICK SHELL MODEL

The thick shell model treats the projectile body as a thick-walled cylindrical conducting shell of outer radius b and inner radius a, being subject to an oscillating uniform field directed along the Y-axis. For a thin shell (see app. A), the axial current density within the shell was treated as uniform and lumped into an equivalent surface current. This caused the phase relation between the inner uniform field and outer induced magnetic dipole to be the same as the spin frequency varied. Additionally, the material magnetic permeability was not included. This will not be the case in the thick shell model, where no uniformity assumption will be made on the axial current density, and the material permeability μ will be included. The B-field will need to be solved within shell's conductive cross section in order to determine the B-field outside and inside the shell. See figure 4 for an illustration of the thick shell model.

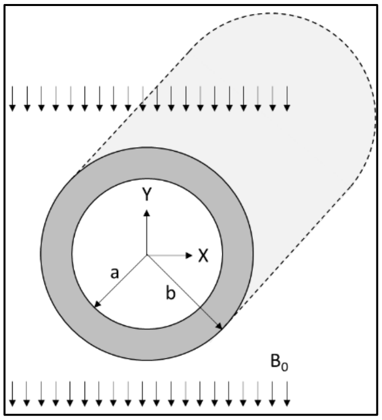

Figure 4
Thick shell model

With aid from reference 5, the field solution for a thick shell of inner radius a and outer radius b subject to an oscillating transverse field will be found. Outside and inside the shell, the magnetic vector potential follows the vector Laplace equation, just as in the thin shell model. Within the shell's conductive material, the A-field is governed by the vector diffusion equation. Again, it can be assumed that all of the components of the A-field other than A_z are zero, yielding the scalar version of the aforementioned equations. These governing scalar equations in all three regions are given as equations 1 through 3:

$$\nabla^2 A_{out} = 0 \tag{1}$$

$$\nabla^2 A_{in} = 0 \tag{2}$$

$$\nabla^2 A_c = \mu\sigma \frac{dA_c}{dt} \tag{3}$$

Equations 1 and 2 are Laplace's equation, and are the governing equations of A_z outside and inside the thick shell, just like in the thin shell model. Equation 3 is the scalar diffusion equation and the governing equation of A_z within the conducting region of the thick shell. The general solutions for all three regions are as in equations 4 through 6:

$$A_{out} = \left(B_o r + \frac{C}{r}\right)\cos(\phi)\, e^{j\omega t} \tag{4}$$

$$A_{in} = \left(Dr\cos(\phi) + E\frac{1}{r}\cos(\phi) + Fr\sin(\phi) + G\frac{1}{r}\sin(\phi)\right) e^{j\omega t} \tag{5}$$

$$A_c = \sum_{\upsilon=-\infty}^{\infty}\big(L\cos(\upsilon\phi) + Msin(\upsilon\phi)\big)\big(NI_\upsilon(\beta r) + PK_\upsilon(\beta r)\big)e^{j\omega t} \tag{6}$$

Where equations 4 and 5 are the same as from the thin shell model, A_{in} must remain finite at $r = 0$; therefore, coefficients E and G are both zero. Equation 6 contains modified Bessel functions and is derived from equation 3 following the steps in appendix C. It is assumed the separation constant υ^2 used in equation C.12 is nonzero and the positive root of equation C.17 is used, yielding the definition of β as shown below in equation 7.

$$\boxed{\beta = \sqrt{j\mu\omega\sigma}} \tag{7}$$

Where μ and σ are the permeability and conductivity of the shell material, and ω is the angular rate of the oscillating $\overrightarrow{B_o}$ field.

The needed boundary conditions at $r = a$ and $r = b$ are given in BC1-BC7. BC1 and BC2 are the boundary conditions of the scalar field A_z, at the $r = a$ and $r = b$ boundaries of the shell, which must be continuous across a boundary. BC3-BC7 are the derivatives of A_z in the r and ϕ directions. These can be derived from the magnetic field boundaries conditions shown in equations 8 and 9:

$$\vec{n} \cdot \left(\vec{B}_{out} - \vec{B}_c\right) = 0 \tag{8}$$

$$\vec{n} \times \left(\frac{\vec{B}_{out}}{\mu_o} - \frac{\vec{B}_c}{\mu}\right) = 0 \tag{9}$$

$$A_{out}|_{r=b} = A_c|_{r=b} \tag{BC-1}$$

$$A_{in}|_{r=a} = A_c|_{r=a} \tag{BC-2}$$

$$\frac{1}{\mu_o}\frac{dA_{out}}{dr}\bigg|_{r=b} = \frac{1}{\mu}\frac{dA_c}{dr}\bigg|_{r=b} \tag{BC-3}$$

$$\frac{1}{\mu_o}\frac{dA_{in}}{dr}\bigg|_{r=a} = \frac{1}{\mu}\frac{dA_c}{dr}\bigg|_{r=a} \tag{BC-4}$$

$$\frac{dA_{out}}{d\phi}\bigg|_{r=b} = \frac{dA_c}{d\phi}\bigg|_{r=b} \tag{BC-5}$$

$$\frac{dA_{in}}{d\phi}\bigg|_{r=a} = \frac{dA_c}{d\phi}\bigg|_{r=a} \tag{BC-6}$$

$$A_{out}(r = \infty) = B_o \mathrm{r} \cos(\phi)\, e^{j\omega t} \tag{BC-7}$$

Where $\vec{n}$ is the normal vector from the conducting shell, which is also the same as $\hat{r}$.

BC7 represents the oscillating uniform B-field and is the same as in the thin shell model. Only BC 1-4 and 7 will be needed.

Using BC1 and BC2, the three general solutions can be combined and solved at their respective boundaries. For A_c and A_{out}, see equations 10 and 11:

$$A_{out}|_{r=b} = \left(B_o b + \frac{C}{b}\right)\cos(\phi)\, e^{j\omega t} \tag{10}$$

$$A_c|_{r=b} = \sum_{\upsilon=-\infty}^{\infty}\left(L\cos(\upsilon\phi) + M sin(\upsilon\phi)\right)\left(NI_\upsilon(\beta b) + PK_\upsilon(\beta b)\right)e^{j\omega t} \tag{11}$$

Equating the two right-hand sides, equating the coefficients of the corresponding cosine terms (hereby removing all values of υ except for $\upsilon = 1$), and dropping the $e^{j\omega t}$ and $\cos(\phi)$ yields as in equation 12:

$$\left(B_o b + \frac{C}{b}\right) = QI_1(\beta b) + RK_1(\beta b) \tag{12}$$

Where M in equation 11 is found to be zero due to no sine terms in equation 10, and L is absorbed into new unknown coefficients Q =LN and R = LP.

For A_{in} and A_c at $r =$, see equations 13 and 14:

$$A_{in}|_{r=a} = (Da\cos(\phi) + Fa\sin(\phi))e^{j\omega t} \tag{13}$$

$$A_c|_{r=a} = L\cos(\phi)\,(NI_1(\beta a) + PK_1(\beta a))e^{j\omega t} \tag{14}$$

Equating the two right-hand sides, it is seen that F in equation 13 is found to be zero as there are no $\sin(\phi)$ terms in equation 14. Dropping $\cos(\phi)\,e^{j\omega t}$ and again absorbing L into new unknown coefficients $Q = LN$ and $R = LP$ yields as in equation 15:

$$Da = QI_1(\beta a) + RK_1(\beta a) \tag{15}$$

Where A_c has become as in equation 16:

$$A_c = (QI_1(\beta r) + RK_1(\beta r))\cos(\phi)\,e^{j\omega t} \tag{16}$$

Applying BC3 to A_{out} and A_c at $r = b$, taking the partial derivative with respect to r, and making use of the recurrence formulas for the derivatives of the modified Bessel functions (ref. 6).

$$\frac{1}{\mu_o}\frac{dA_{out}}{dr}\bigg|_{r=b} = \frac{1}{\mu}\frac{dA_c}{dr}\bigg|_{r=b} \tag{17}$$

$$\frac{1}{\mu_o}\left(B_o - \frac{C}{b^2}\right)\cos(\phi)\,e^{j\omega t} = \frac{1}{\mu}\left(Q\frac{d}{dr}I_1(\beta r) + R\frac{d}{dr}K_1(\beta r)\right)\cos(\phi)\,e^{j\omega t}\bigg|_{r=b} \tag{18}$$

$$\frac{\mu}{\mu_o}\left(B_o - \frac{C}{b^2}\right) = Q\beta\left(\frac{1}{\beta b}I_1(\beta b) + I_2(\beta b)\right) + R\beta\left(\frac{1}{\beta b}K_1(\beta b) - K_2(\beta b)\right) \tag{19}$$

$$\frac{\mu}{\mu_o}\left(B_o - \frac{C}{b^2}\right) = Q(\frac{1}{b}I_1(\beta b) + \beta I_2(\beta b)) + R\left(\frac{1}{b}K_1(\beta b) - \beta K_2(\beta b)\right) \tag{20}$$

$$\frac{\mu}{\mu_o}\left(B_o - \frac{C}{b^2}\right) = \frac{1}{b}\left(QI_1(\beta b) + RK_1(\beta b)\right) + Q\beta I_2(\beta b) - R\beta K_2(\beta b) \tag{21}$$

Substituting the first term on the right-hand side yields

$$\frac{\mu}{\mu_o}\left(B_o - \frac{C}{b^2}\right) = \left(B_o + \frac{C}{b^2}\right) + Q\beta I_2(\beta b) - R\beta K_2(\beta b) \tag{22}$$

$$-\left(1 + \frac{\mu}{\mu_o}\right)\frac{C}{b^2} = Q\beta I_2(\beta b) - R\beta K_2(\beta b) + \left(1 - \frac{\mu}{\mu_o}\right)B_o \tag{23}$$

Applying BC4 to A_{in} and A_c at $r = a$ and again performing the partial derivatives and making use of recurrence formulas

$$\frac{1}{\mu_o}\frac{dA_{in}}{dr}\bigg|_{r=a} = \frac{1}{\mu_o}D\cos(\phi)\,e^{j\omega t} = \frac{1}{\mu}\frac{dA_c}{dr}\bigg|_{r=a} = Q\beta I_1{}'(\beta r) + R\beta K_1{}'(\beta r)|_{r=a}\frac{1}{\mu}\cos(\phi)\,e^{j\omega t} \tag{24}$$

$$\frac{\mu}{\mu_o}D = Q\beta\left(\frac{1}{\beta a}I_1(\beta a) + I_2(\beta a)\right) + R\,\beta(\frac{1}{\beta a}K_1(\beta a) - K_2(\beta a)) \tag{25}$$

$$\frac{\mu}{\mu_o}D = Q\frac{1}{a}I_1(\beta a) + Q\beta I_2(\beta a) + R\frac{1}{a}K_1(\beta a) - R\beta K_2(\beta a) \tag{26}$$

One can substitute from equation 15 the terms $Q\frac{1}{a}I_1(\beta a)$ and $R\frac{1}{a}K_1(\beta a)$ with simply D, yielding after some rearranging

$$Q\beta I_2(\beta a) = R\beta K_2(\beta a) + D(\frac{\mu}{\mu_o} - 1) \tag{27}$$

At this point, there are four equations for the four unknown coefficients C, Q, R, and D repeated in equations 28 through 31:

$$\left(B_o b + \frac{C}{b}\right) = QI_1(\beta b) + RK_1(\beta b) \tag{28}$$

$$-\left(1 + \frac{\mu}{\mu_o}\right)\frac{C}{b^2} = Q\beta I_2(\beta b) - R\beta K_2(\beta b) + \left(1 - \frac{\mu}{\mu_o}\right)B_o \tag{29}$$

$$Da = QI_1(\beta a) + RK_1(\beta a) \tag{30}$$

$$Q\beta I_2(\beta a) = R\beta K_2(\beta a) + D(\frac{\mu}{\mu_o} - 1) \tag{31}$$

Solving for Q in terms of R using equations) and) yields equation 32:

$$Q = R\frac{\left(a\beta K_2(\beta a) + K_1(\beta a)(\frac{\mu}{\mu_o} - 1)\right)}{\left(a\beta I_2(\beta a) - I_1(\beta a)(\frac{\mu}{\mu_o} - 1)\right)} \tag{32}$$

To make notation easier, the previous fraction will be represented by ζ equation

$$\boxed{\zeta = \frac{a\beta K_2(\beta a) + K_1(\beta a)(\frac{\mu}{\mu_o} - 1)}{a\beta I_2(\beta a) - I_1(\beta a)(\frac{\mu}{\mu_o} - 1)}} \tag{33}$$

$$Q = R\zeta \tag{34}$$

Substituting away Q in equation 28 with 34 and factoring out R yields

$$\left(B_o b + \frac{C}{b}\right) = R(\zeta I_1(\beta b) + K_1(\beta b)) \tag{35}$$

$$-\left(1 + \frac{\mu}{\mu_o}\right)\frac{C}{b^2} = R\beta(\zeta I_2(\beta b) - K_2(\beta b)) + \left(1 - \frac{\mu}{\mu_o}\right)B_o \tag{36}$$

$$Da = R(\zeta I_1(\beta a) + K_1(\beta a)) \tag{37}$$

Then introduce the following three substitutions for the right-hand side multiplicands of R

$$\boxed{\tau = \zeta I_1(\beta b) + K_1(\beta b)} \tag{38}$$

$$\boxed{\alpha = \zeta I_2(\beta b) - K_2(\beta b)} \tag{39}$$

$$\boxed{\Omega = \zeta I_1(\beta a) + K_1(\beta a)} \tag{40}$$

This simplifies the equations for the unknown coefficients to:

$$B_o b + \frac{C}{b} = \tau R \tag{41}$$

$$-\left(1 + \frac{\mu}{\mu_o}\right)\frac{C}{b^2} = \alpha R\beta + \left(1 - \frac{\mu}{\mu_o}\right)B_o \tag{42}$$

$$Da = \Omega R \tag{43}$$

Hence, one can solve for C, D, and Q to yield the coefficients for the outer induced dipole, the interior uniform field, and the field within the sidewall. They are:

$$\boxed{C = \frac{-\frac{\alpha}{\tau}\beta b^3 + \left(\frac{\mu}{\mu_o} - 1\right) b^2}{\left(1 + \frac{\mu}{\mu_o}\right) + \frac{\alpha}{\tau}\beta b} B_o} \tag{44}$$

$$\boxed{D = \left(b + \frac{-\frac{\alpha}{\tau}\beta b^2 + \left(\frac{\mu}{\mu_o} - 1\right) b}{\left(1 + \frac{\mu}{\mu_o}\right) + \frac{\alpha}{\tau}\beta b}\right) \frac{\Omega}{\alpha\tau} B_o} \tag{45}$$

$$\boxed{Q = \left(b + \frac{-\frac{\alpha}{\tau}\beta b^2 + \left(\frac{\mu}{\mu_o} - 1\right) b}{\left(1 + \frac{\mu}{\mu_o}\right) + \frac{\alpha}{\tau}\beta b}\right) \frac{\zeta}{\tau} B_o} \tag{46}$$

Solutions for A_{out}, A_{in}, and A_c are:

$$\boxed{A_{out} = \left(B_o r + \frac{C}{r}\right) \cos(\phi)\, e^{j\omega t}} \tag{47}$$

$$\boxed{A_{in} = D r \cos(\phi)\, e^{j\omega t}} \tag{48}$$

$$\boxed{A_c = Q \left(I_1(\beta r) + \frac{K_1(\beta r)}{\zeta}\right) \cos(\phi)\, e^{j\omega t}} \tag{49}$$

$B = \nabla x A$ in polar coordinates is:

$$\vec{B} = \frac{1}{r}\frac{dA}{d\phi}\hat{r} - \frac{dA}{dr}\hat{\phi} \tag{50}$$

The B-field outside, inside, and within the material of the conducting shell are

$$\boxed{\vec{B}_{out} = -\left(B_o + \frac{C}{r^2}\right) \sin(\phi)\, e^{j\omega t}\hat{r} + \left(-B_o + \frac{C}{r^2}\right) \cos(\phi)\, e^{j\omega t}\hat{\phi}} \tag{51}$$

$$\boxed{\vec{B}_{in} = -D \sin(\phi) e^{j\omega t}\, \hat{r} - D \cos(\phi)\, e^{j\omega t}\hat{\phi}} \tag{52}$$

$$\boxed{\vec{B}_c = \frac{-Q}{r}\left(I_1(\beta r) + \frac{K_1(\beta r)}{\zeta}\right) \sin(\phi)\, e^{j\omega t}\hat{r} - Q\beta \left(I_0(\beta r) - \frac{I_1(\beta r)}{\beta r} - \frac{K_0(\beta r)}{\zeta} - \frac{K_1(\beta r)}{\zeta\beta r}\right) \cos(\phi)\, \hat{\phi}} \tag{53}$$

With β, C, D, and Q previously defined using τ, α, Ω , ζ and where the recursive relations were used $\frac{dI_1}{dz} = I_0(z) - \frac{1}{z} I_1(z)$ and $\frac{dK_1}{dz} = -K_0(z) - \frac{1}{z} K_1(z)$ (ref. 6).

The induced outer dipole can be viewed as the sum of two dipoles, one due to the eddy currents in the shell wall (from the leftmost term of the numerator of C), and one due to magnetic polarization of the shell wall material (from the rightmost term of the numerator of C). As $\omega \rightarrow \infty$, $C \rightarrow -b^2 B_o$, forming an induced diamagnetic dipole that acts to buck out the external field from the cylinder. As $\omega \rightarrow 0$ and $\mu \gg \mu_o$, $C \rightarrow b^2 B_o$ forms an induced paramagnetic dipole that is aligned with the external field. In the case where $\mu = \mu_o$, such as for non-magnetic metals, no paramagnetic dipole is formed, and the coefficient C is similar to that in the thin shell model, only with two $\frac{\alpha}{\tau}$ correction terms included and being a function of

$\beta = \sqrt{j\mu\omega\sigma}$ instead of $\delta = \mu_0 \omega \sigma \Delta$.

The D coefficient is very different from the thin shell model. Here there are extra terms that will vary with ω, yielding a difference in the amplitude and phase between the outer dipole and inner field. This is due to the inclusion of magnetic diffusion through the conductive region of the thick shell. In both models, as $\omega \to \infty$, $D \to 0$, yielding no field amplitude within the cylinder. For the thick shell model, in the case where $\omega \to 0$ or $\sigma \to 0$ and $\mu = \mu_o$, $D \to B_o \frac{b}{a}\frac{\Omega}{\tau}$ and $\frac{\Omega}{\tau} \to \frac{a}{b}$. Hence, $D \to B_o$, creating an interior uniform field that is the same as the external field. This is as if the cylinder isn't there, which should be the case for conductive non-spinning and non-magnetic materials, or nonconductive materials.

Using a 155-mm outer diameter cylinder as an example, in both aluminum and steel, with 10-mm wall thickness ($a = 67.5\ mm, b = 77.5\ mm$), subject to a rotating transverse field, the normalized magnitude and phase angle of the induced outer dipole and the interior field, from 0.1 to 1000 Hz, are plotted in figure 5. The dipole magnitude is normalized to $b^2 B_o$ and the interior field is normalized to B_o.

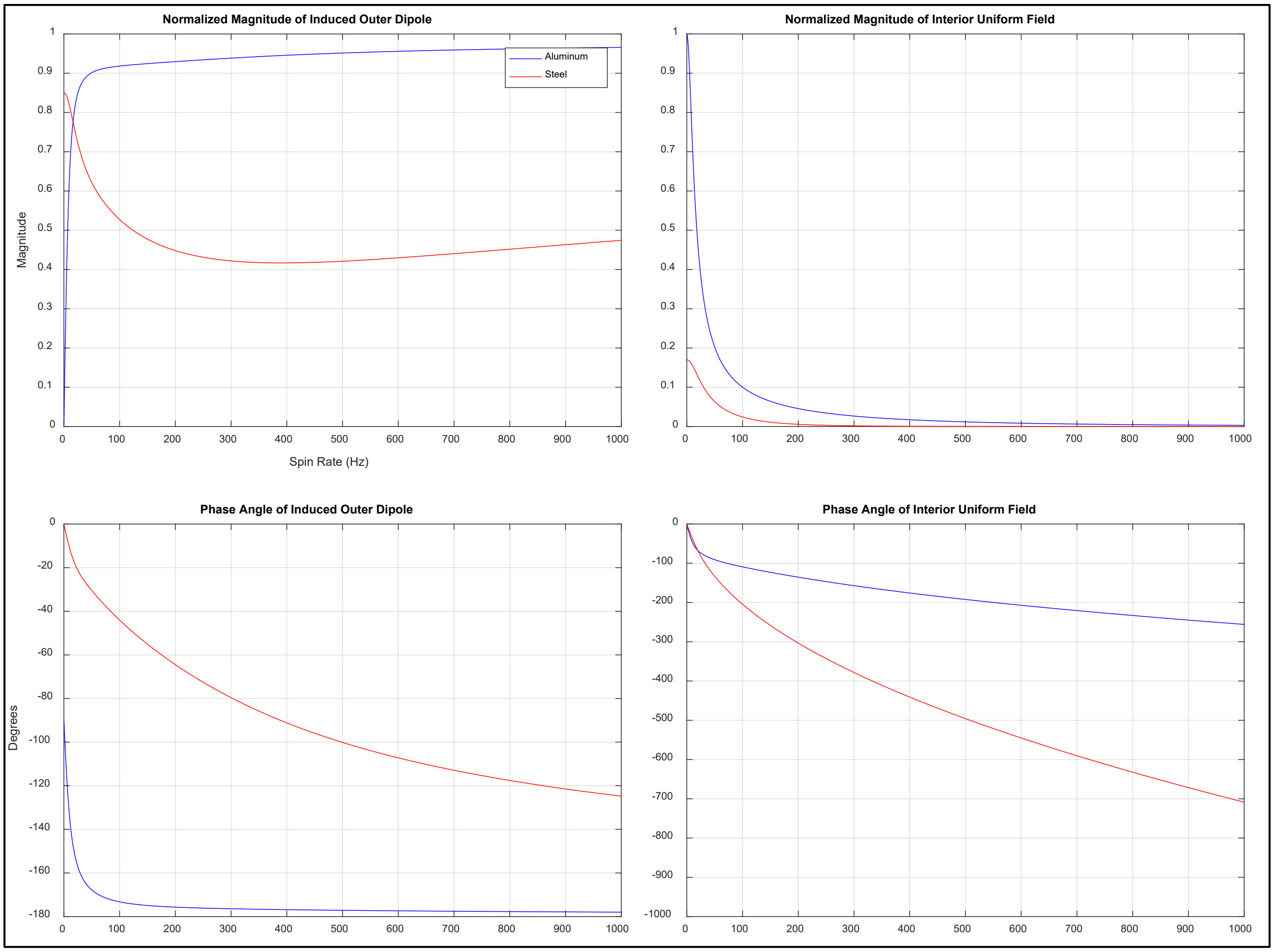

Figure 5
Plots of normalized magnitude and phase angle of the induced outer dipole and the interior field, from 0.1 to 1000 Hz

Plots of the B-field with the example cylinder in both aluminum and steel are shown in figures 6 through 9. Figures 6 and 7 show the field around the cylinders as rotation is varied from 0.1 to 400 Hz and observed at zero phase angle. Figures 8 and 9 show the field with a fixed spin rate of 300 Hz, at a phase angle of 0 to 315 deg.

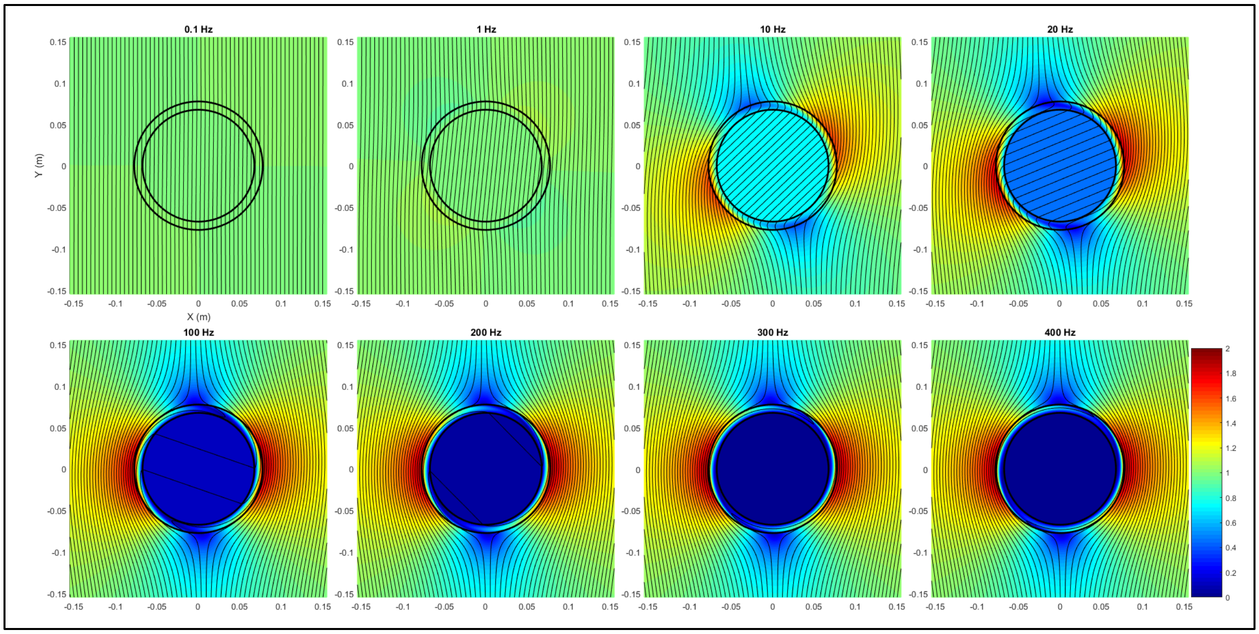

Figure 6
Aluminum example cylinder, 0.1 to 400 Hz rotating field at phase = 0

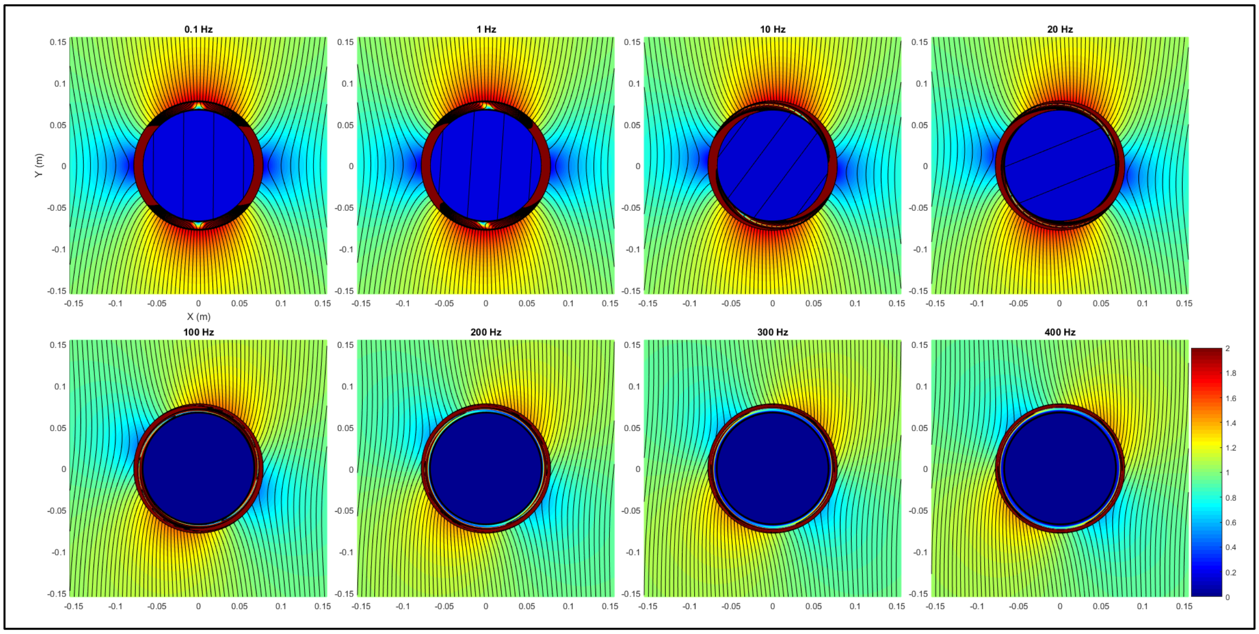

Figure 7
Steel example cylinder, 0.1 to 400 Hz rotating field at phase = 0

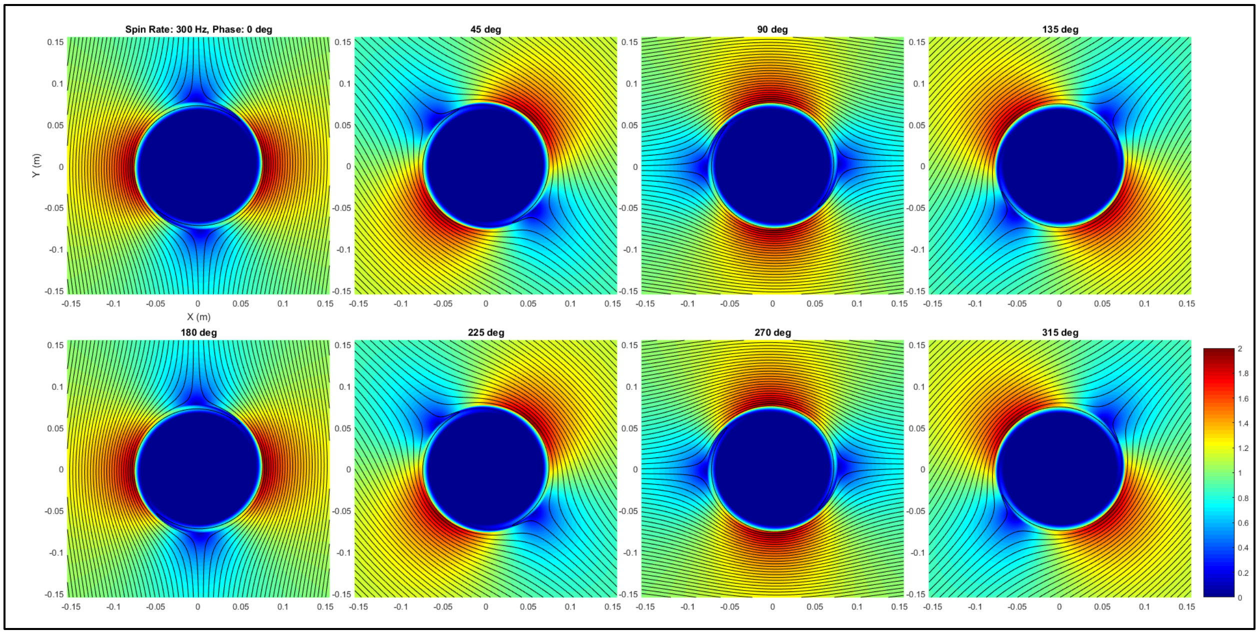

Figure 8
Aluminum example cylinder, 300 Hz rotating field, at phase angles 0 to 315 deg

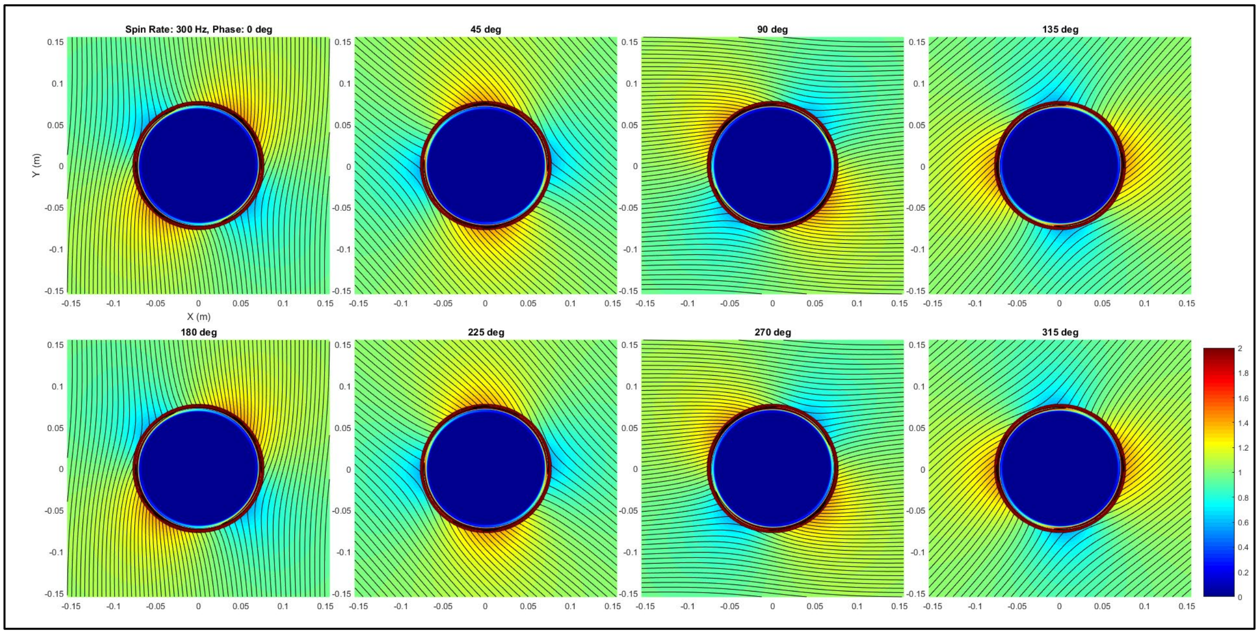

Figure 9
Steel example cylinder, 300 Hz rotating field, at phase angles 0 to 315 deg

ROLL ANGLE MEASUREMENTS

With a-priori knowledge of the geomagnetic field vector, a smart projectile equipped with a magnetometer can estimate its roll angle relative to the field by measuring the ratio of the components of $\vec{B}_t$. Define the projectile true and measured roll angles as:

$$\Phi_{\text{true}} = -\left(\omega t + \frac{\pi}{2}\right) \tag{54}$$

$$\Phi_{\text{measured}} = \arctan(Re\{\frac{Bmeasured_\phi}{Bmeasured_r}\}) \tag{55}$$

Using the thick shell model equations for $\vec{B}_{out}$, adapted for a uniform rotating field using appendix D, the following equation can be created:

$$\Phi_{\text{measured}} = \arctan\left(Re\{\frac{\left(-B_o+\frac{C}{r^2}\right)\cos(\phi)e^{j\omega t}+\left(-B_o+\frac{C}{r^2}\right)\cos\left(\phi+\frac{\pi}{2}\right)e^{j\left(\omega t+\frac{\pi}{2}\right)}}{-\left(B_o+\frac{C}{r^2}\right)\sin(\phi)e^{j\omega t}+-\left(B_o+\frac{C}{r^2}\right)\sin\left(\phi+\frac{\pi}{2}\right)e^{j\left(\omega t+\frac{\pi}{2}\right)}}\}\right) \tag{56}$$

Which for a magnetometer placed at $\phi = 0$ simplifies to

$$\boxed{\Phi_{\text{measured}} = \arctan\left(\frac{B_o\cos(\omega t)-\frac{C_m}{r^2}\cos(\omega t+\angle C)}{B_o\sin(\omega t)+\frac{C_m}{r^2}\sin(\omega t+\angle C)}\right)} \tag{57}$$

For a slowly spinning, magnetic material, $\rightarrow b^2 B_o$, yielding

$$\Phi_{\text{measured}} = \arctan\left(\frac{(r^2-b^2)\cos(\omega t)}{(r^2+b^2)\sin(\omega t)}\right) \tag{58}$$

And for a fast spinning cylinder, $C \rightarrow -b^2 B_o$, yielding

$$\Phi_{\text{measured}} = \arctan\left(\frac{(r^2+b^2)\cos(\omega t)}{(r^2-b^2)\sin(\omega t)}\right) \tag{59}$$

The roll angle error ($\Phi_{\text{measured}} - \Phi_{\text{true}}$) becomes a periodic function of Φ_{true} . A comparison of Φ_{measured} versus Φ_{true} for various spin frequencies is given in the left-most columns of figures 10 and 11, for an aluminum and steel example cylinder, respectively (Φ_{true} is plotted in black).

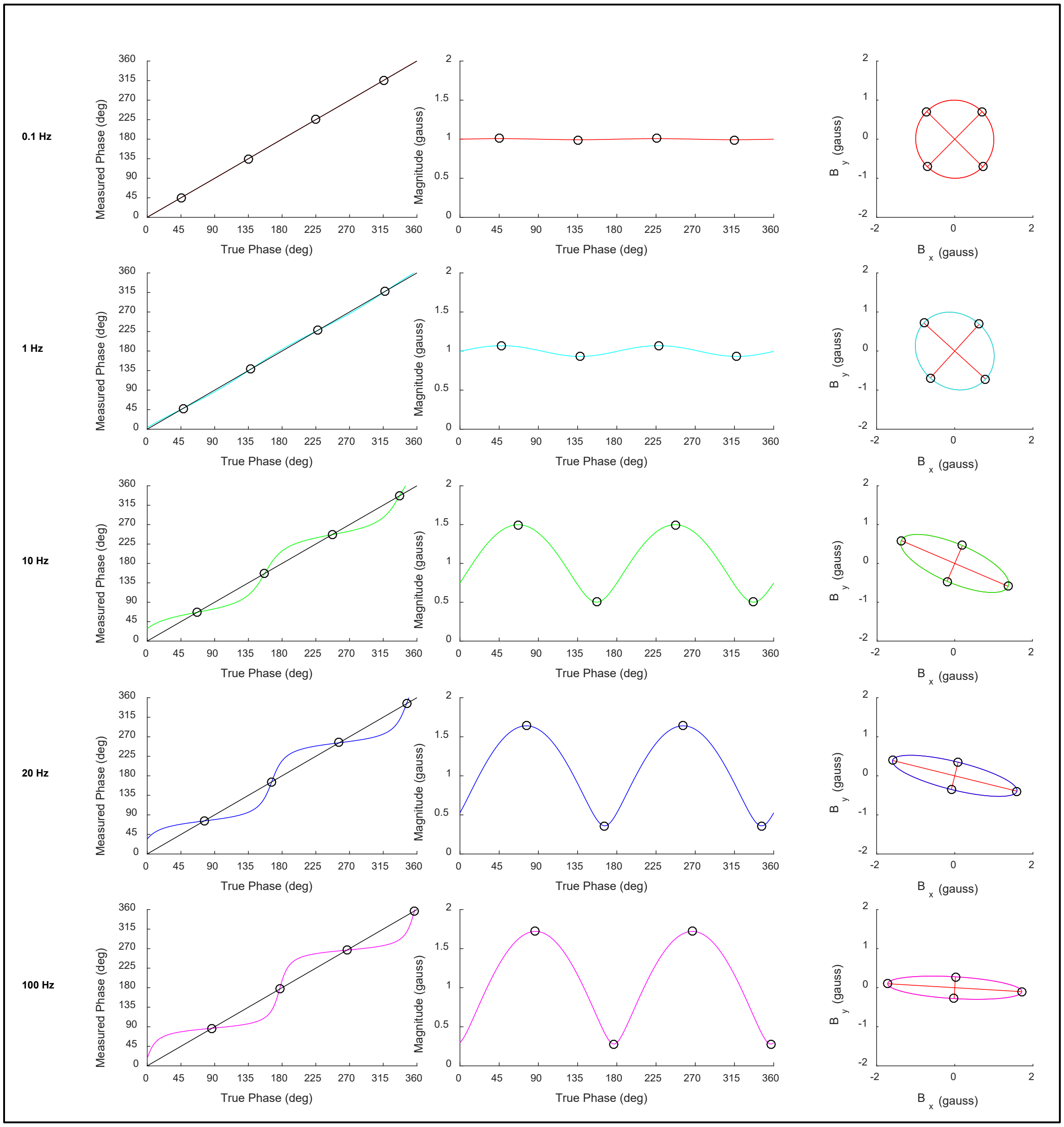

Note: (left) Φ_{measured} and Φ_{true} (black) versus Φ_{true}, (middle) magnitude of $Bmeasured$ with maximum and minimum marked, (right) $Bmeasured_{\phi}$ versus $Bmeasured_{r}$, with $Bmeasured$ with maximum and minimum marked, and best-fit ellipse minor and major axes.

Figure 10
Aluminum example cylinder, observed 1 cm outside of the shell

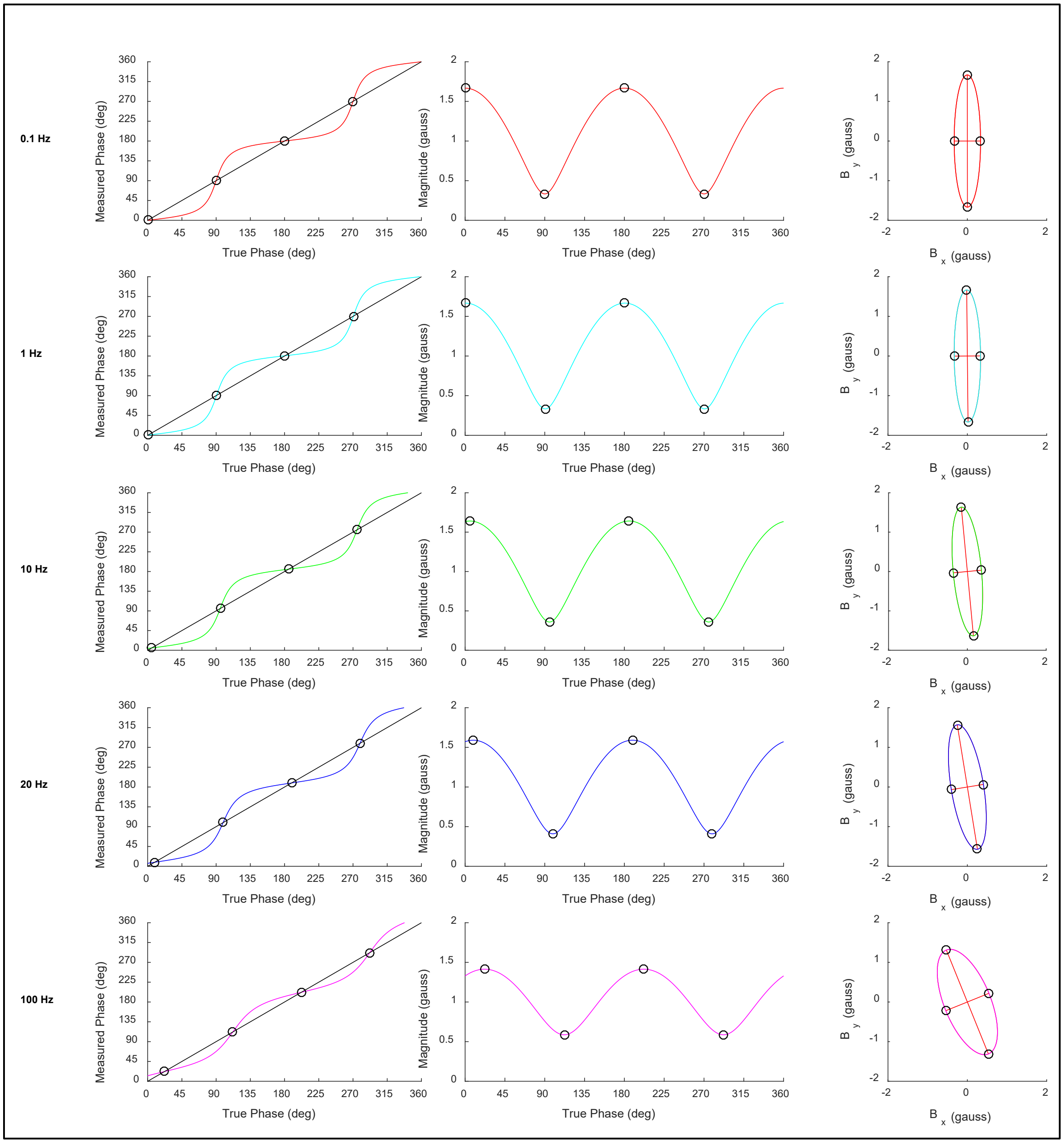

Note: (left) Φ_{measured} and Φ_{true} (black) versus Φ_{true}, (middle) magnitude of $Bmeasured$ with maximum and minimum marked, (right) $Bmeasured_{\phi}$ versus $Bmeasured_{r}$, with $Bmeasured$ with maximum and minimum marked, and best-fit ellipse minor and major axes.

Figure 11
Steel example cylinder, observed 1 cm outside of the shell

Importantly, the roll error becomes zero when the magnitude of $Bmeasured$ is maximum and minimum. This magnitude is plotted in the middle column of figures 10 and 11, with the maximum and minimum values marked with black circles. The locus of points for $Bmeasured_{\phi}$ and $Bmeasured_{r}$ are plotted in the right-most columns for the aforementioned figures, with the same magnitude maximum and minimum circle markings.

Recognizing that the numerator and denominator of the fraction in equation 57 can be treated as the parametric equations for a tilted ellipse, tilted at angle $\angle C$. Best-fit ellipse methods can be used to recover ωt, and hence Φ_{true} from Φ_{measured}. A best-fit ellipse routine was used on the points in the right-most columns of the aforementioned figures, with major and minor axes plotted. These axes intersect the maximum and minimum markers.

Note that in the case of nonconductive, nonmagnetic shell material, or with a magnetometer far away from the shell, no dipole formed at all, and in equation 60:

$$\Phi_{\text{measured}} = -\frac{\pi}{2} - \omega\text{t} = \Phi_{\text{true}} \tag{60}$$

If the magnetometer is placed inside the shell (eqs. 61 through 63)

$$\vec{B}_{in} = -D\sin(\phi)e^{j\omega t}\,\hat{r} - D\cos(\phi)\,e^{j\omega t}\hat{\phi} \tag{61}$$

$$\Phi_{\text{measured}} = -\frac{\pi}{2} - \omega\text{t} - \angle D \tag{62}$$

$$\boxed{\Phi_{\text{measured}} = \Phi_{\text{true}} - \angle D} \tag{63}$$

The measured roll angle will be angular-shifted from the true roll angle. This is referred to as the distortion angle γ_D in reference 4.

COMPARISON WITH TWO-DIMENSIONAL FINITE ELEMENT ANALYSIS MODELING

The aluminum and steel example cylinder was imported into ANSYS Electronics Desktop 2018 (also known as Ansoft Maxwell) as a way to validate the thick shell model. The outer boundary of the model was a 4-m diameter circle of a complex vector potential boundary condition, creating a counter-clockwise rotating 1 gauss B-field. The thick shell model was implemented in MATLAB using the same cylinder dimensions in both aluminum and steel, also creating a counter-clockwise rotating 1 gauss B-field. The B-field was evaluated in Maxwell as a 2D eddy current solution and MATLAB. Evaluation was performed at zero phase (i.e., time = 0 sec) and at two points: center (0 mm, 0 mm) and outside (87.5 mm, 0 mm) along the X-axis. The results are given in table 2. Both the Maxwell model and MATLAB model agree on the normalized B-field magnitude to two decimal places at both points. The B-field angles also agree to within 0.1 deg at both points. Plots of the Maxwell models are shown in figures 12 and 13.

Table 2
Comparison of Ansoft Maxwell and MATLAB models

Aluminum shell; point at center; at phase 0				
Frequency	Magnitude (norm)		Angle (By/Bx)	
	Maxwell	MATLAB	Maxwell	MATLAB
0.1	1.0000	1.0000	-90.5736	-90.5737
1	0.9955	0.9954	-95.7195	-95.7201
10	0.7223	0.7222	-136.2782	-136.2792
20	0.4625	0.4624	-157.4968	-157.4913
100	0.1002	0.1002	160.8514	160.9020
200	0.0455	0.0456	134.5604	134.6537
300	0.0265	0.0265	112.8478	112.9717
400	0.0171	0.0171	94.1252	94.2717
Aluminum shell; point outside; at phase 0				
0.1	1.0001	1.0001	-90.3953	-90.3957
1	1.0089	1.0089	-93.8859	-93.8899
10	1.3930	1.3921	-105.0099	-105.0318
20	1.5959	1.5943	-100.7533	-100.7714
100	1.7197	1.7174	-92.8236	-92.8276
200	1.7303	1.7280	-91.8203	-91.8218
300	1.7377	1.7354	-91.5208	-91.5218
400	1.7437	1.7413	-91.3514	-91.3523
Steel shell; point at center; at phase 0				
0.1	0.1695	0.1698	-90.3800	-90.3794
1	0.1693	0.1696	-93.7988	-93.7929
10	0.1555	0.1559	-126.7499	-126.6959
20	0.1271	0.1275	-158.0184	-157.9287
100	0.0241	0.0242	65.4960	65.7097
200	0.0054	0.0055	-33.6500	-33.3360
300	0.0017	0.0017	-108.6796	-108.2837
400	0.0006	0.0006	-171.3835	-170.9132
Steel shell; point outside; at phase 0				
0.1	0.3324	0.3328	-90.2305	-90.2310
1	0.3331	0.3335	-92.2979	-92.3027
10	0.3886	0.3891	-107.8520	-107.8945
20	0.4770	0.4777	-112.9085	-112.9709
100	0.7583	0.7590	-112.2116	-112.2621
200	0.9052	0.9058	-110.4558	-110.4977
300	0.9946	0.9951	-109.0587	-109.0952
400	1.0581	1.0585	-107.9531	-107.9859

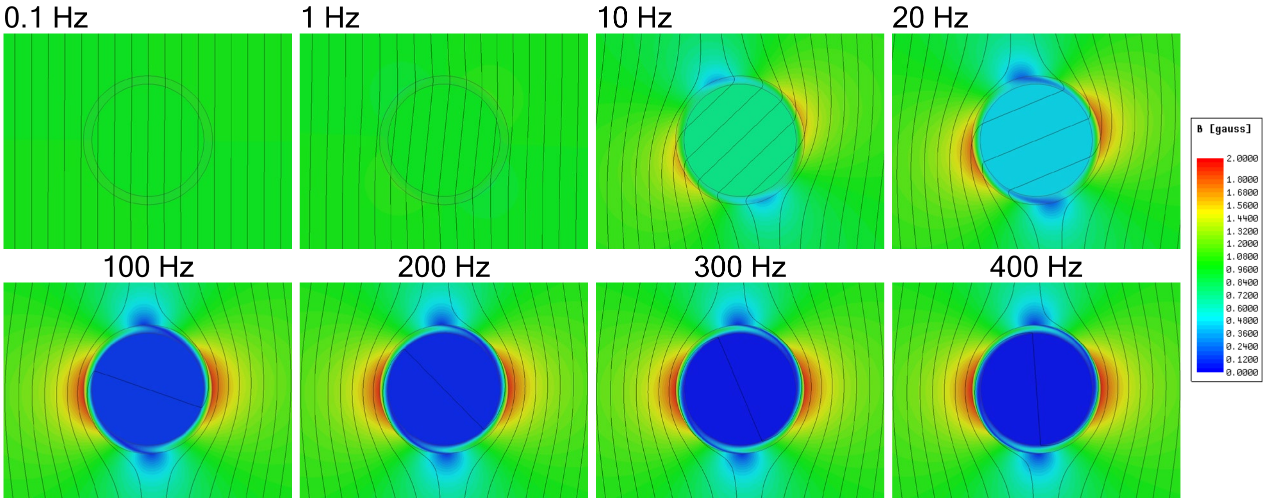

Figure 12
2D Ansoft Maxwell model of aluminum example cylinder

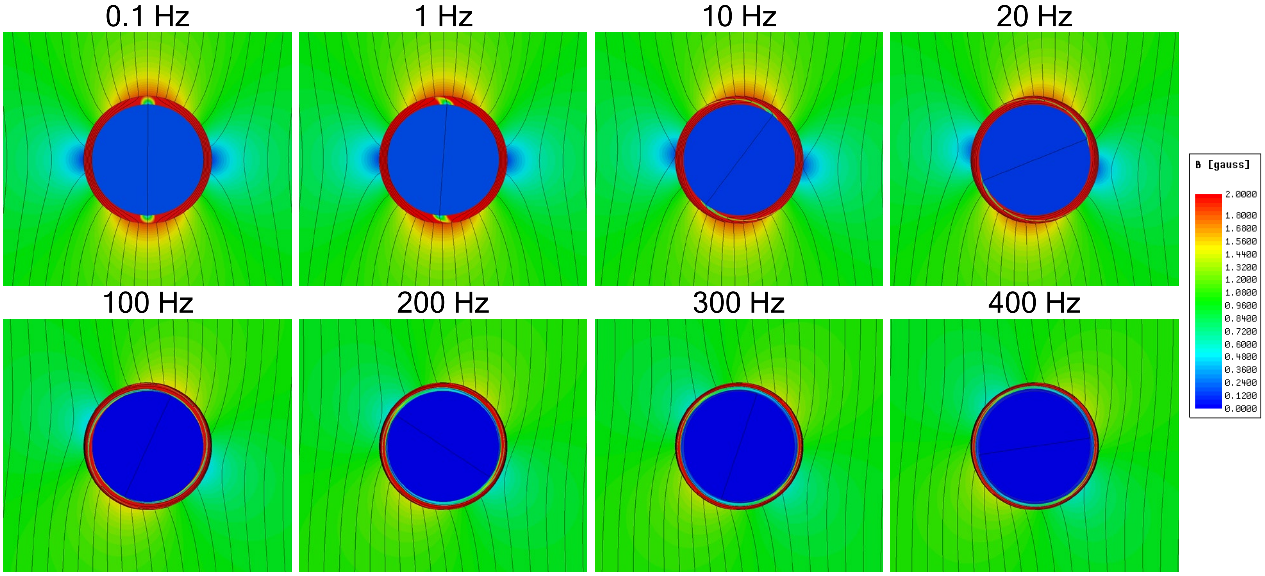

Figure 13
2D Ansoft Maxwell model of steel example cylinder

VARIATION WITH TEMPERATURE

Temperature affects the conductivity of the shell material through its temperature coefficient. The resistivity of aluminum has a positive temperature coefficient, yielding conductivity as per equation 64, where α_r is the temperature coefficient of the resistivity of the metal:

$$\sigma = \frac{\sigma_{ref}}{1+\alpha_r(T-T_{ref})} \tag{64}$$

For aluminum, as the temperature of the metal increases from -55 to 125 °C, the conductivity σ of the metal will vary from 141% of the original σ_{ref} at 20 °C down to 71%.

The effects of this change in conductivity on the induced outer dipole and the total interior uniform field for the thick shell model of a 155-mm outer diameter, 10-mm wall thickness cylinder in the aluminum are plotted in figure 14.

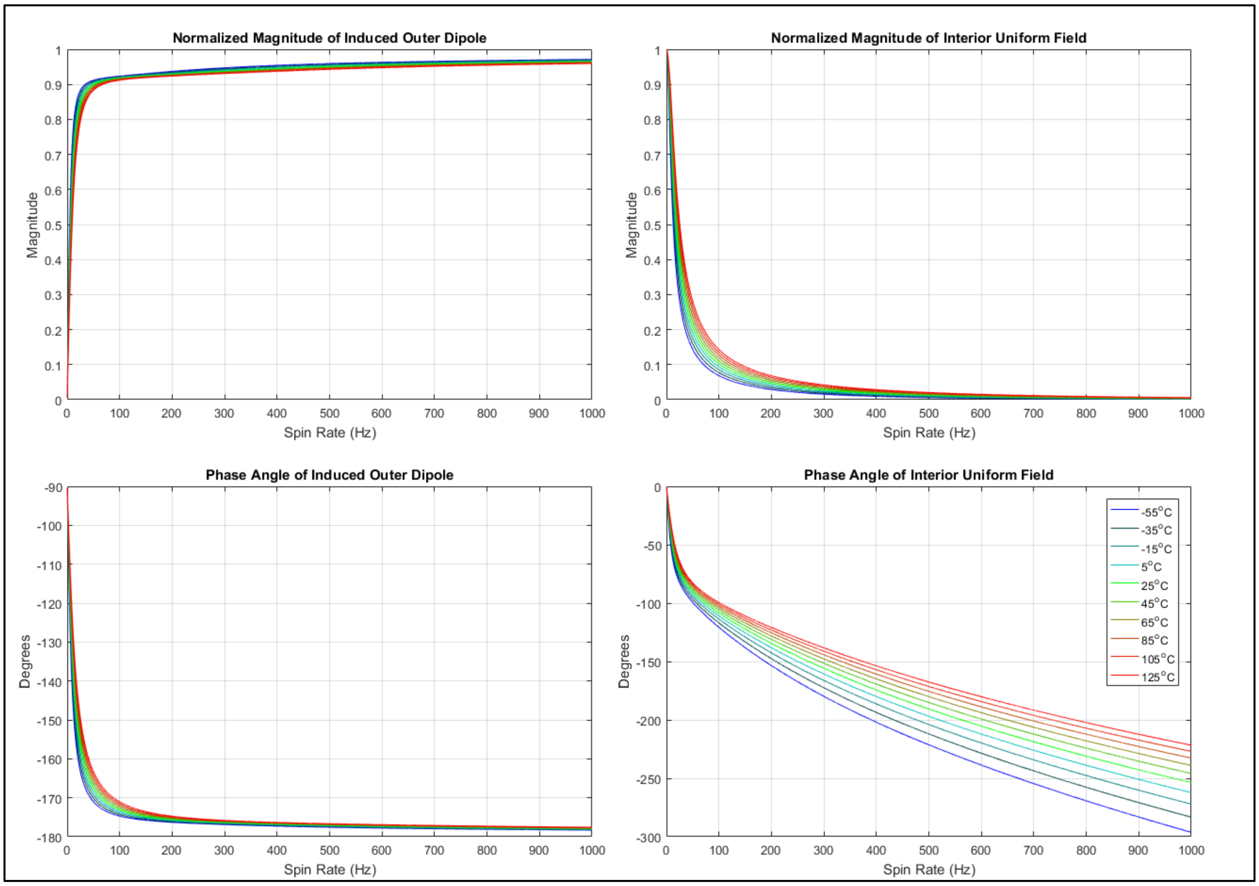

Figure 14
Plots of normalized magnitude and phase angle of the induced outer dipole and the interior field for an aluminum example cylinder, from 0.1 to 1000 Hz, from -55 to 125 °C

For an aluminum cylinder, between 200 to 300 Hz and also between -55 to 125 °C, the phase angle of the outer induced dipole varies between -176.9 and -174.7 deg, a difference of 2.2 deg. The phase angle of the total interior field varies between -179.9 and -120.9 deg, a difference of 59 deg, which is significantly greater. The effects of this change in conductivity on a steel cylinder are plotted in figure 15.

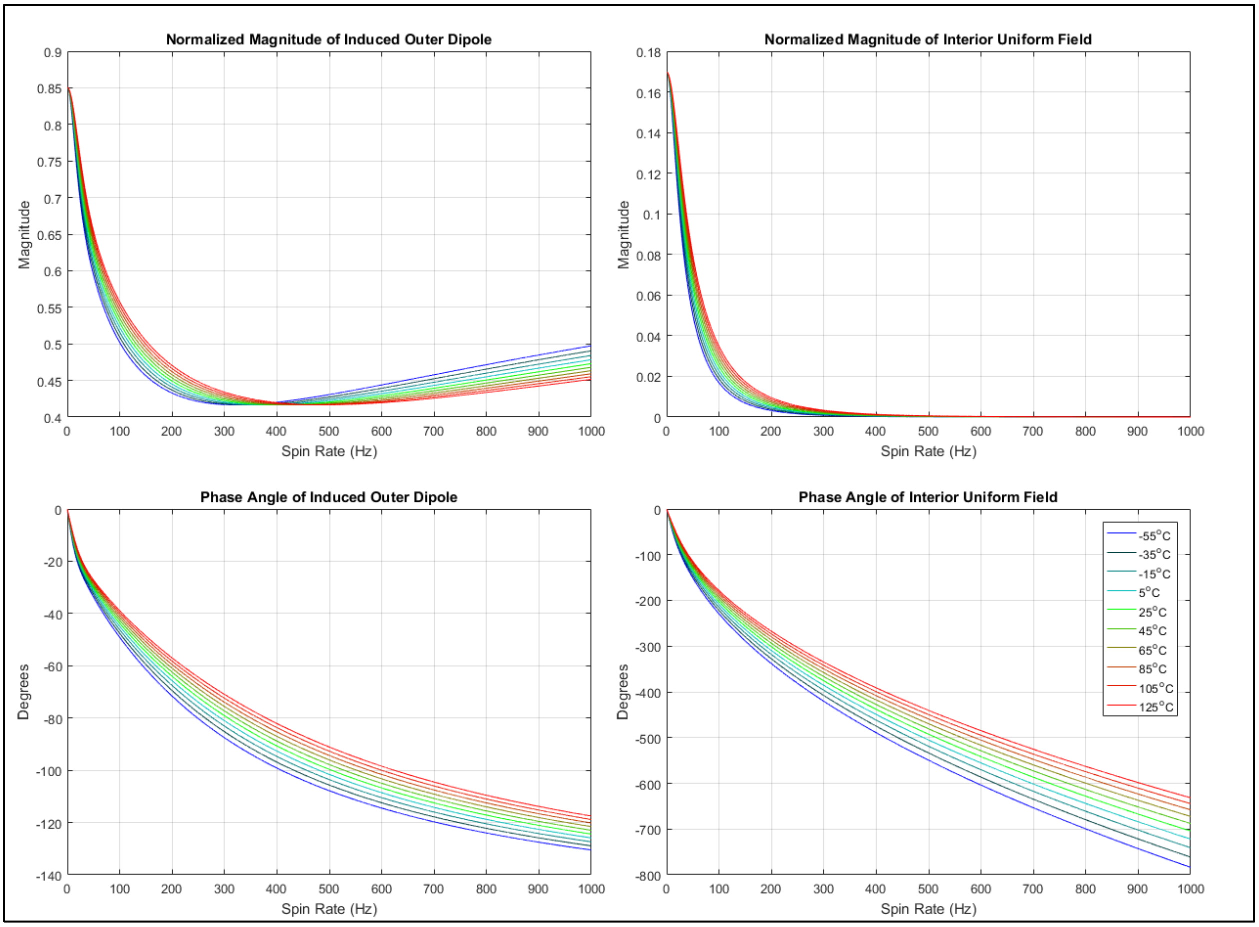

Figure 15
Plots of normalized magnitude and phase angle of the induced outer dipole and the interior field for a steel example cylinder, from 0.1 to 1000 Hz, from -55 to 125 °C

For a steel cylinder, between 200 to 300 Hz and also between -55 to 125 °C, the phase angle of the outer induced dipole varies between -57 and -87.6 deg, a difference of 30.6 deg. The phase angle of the total interior field varies between -267.6 and -420.6 deg, a difference of 153 deg, which is, again, significantly greater.

COMPARISON WITH THREE-DIMENSIONAL FINITE CYLINDER FINITE ELEMENT ANALYSIS MODELING

The thick shell model treats the geometry of the projectile as if it were a hollow cylinder of infinite extent. The results obtained are expected to be valid for a magnetometer placed midway on a cylinder of finite-length, provided that the cylinder is long enough. This can be explored using 3D FEA magnetic modeling, where one can create a virtual finite-length cylinder in a rotating transverse B-field and explore the nearby field behavior while the cylinder's length is varied.

A 3D version of the aluminum and steel example cylinder was created as a harmonic eddy current solution in ANSYS Electronics Desktop, subject to a rotating transverse B-field, of 1 gauss magnitude, rotating at 300 Hz. The field was initially directed along the -Y axis and rotates within the XY plane. The cylinder had an outer diameter of 155 mm, wall thickness of 10 mm, was closed at both ends, and was directed along the Z axis, as shown in figure 16. The cylinder was surrounded by a vacuum region, with 700-mm padding in all directions, and complex Tangential-H field boundary conditions on its outer faces to create the rotating field. The side wall of the cylinder was layered at 1-mm intervals to force the FEA mesher to create a detailed mesh within the conducting region.

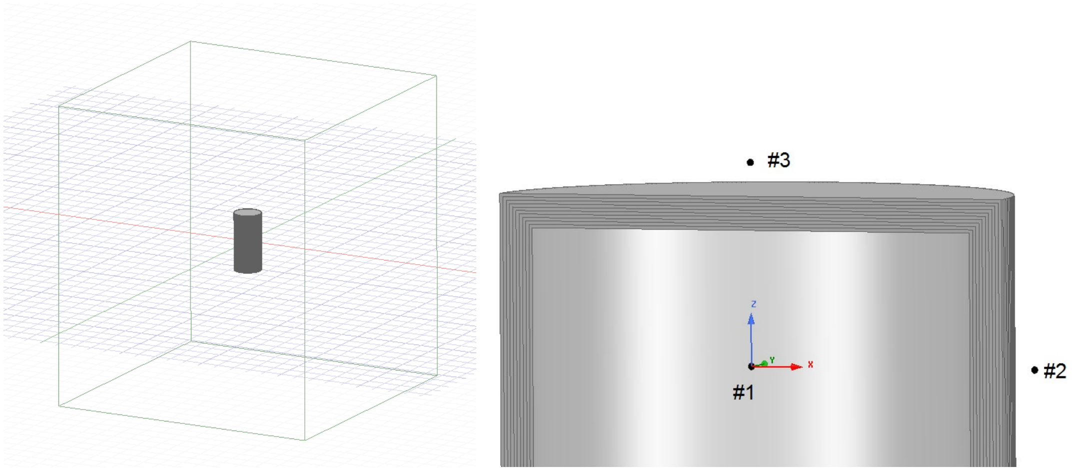

Figure 16
Geometry of 3D FEA model – full model (left) and cylinder showing layering and evaluation points no. 1, 2, 3 (right)

The length of the cylinder was varied from 30 to 2,000 mm, and the fields were measured at three points: point 1, "Center" (X=0, Y=0, Z=0) which is the origin and is within the cylinder's center cavity; point 2, "Outside" (87.5 mm, 0, 0) which is midway along the cylinder length and 10 mm outside its outer radius; and point 3, "Top" (0,0,Length/2+1 cm) which is 10 mm above the cylinder end and along its rotational axis. The magnitude and direction of the $\vec{B}_x$ and $\vec{B}_y$ components for the aluminum case are shown in figure 17, where results are also compared to the infinite length 2D FEA model.

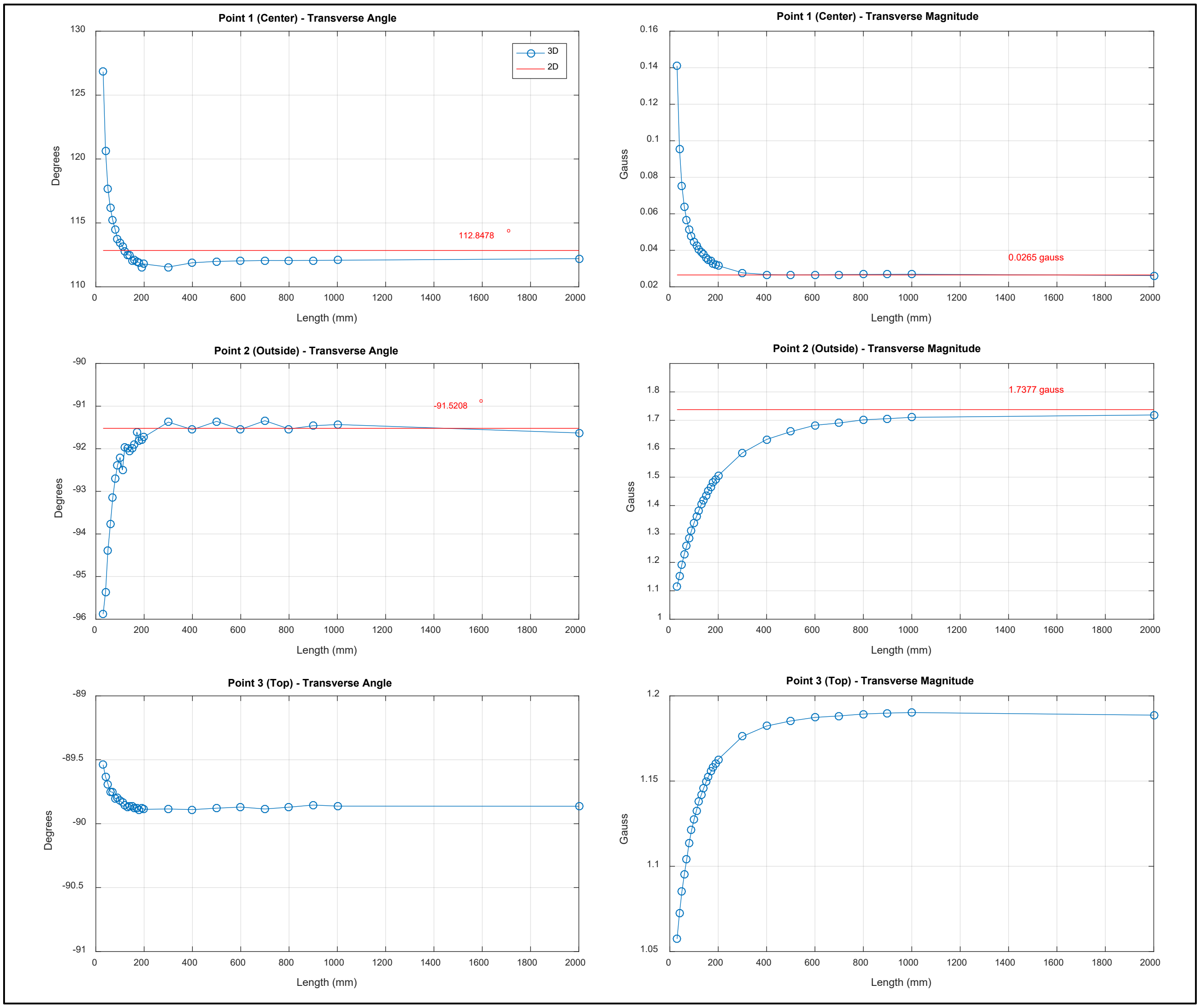

Figure 17
Aluminum cylinder varying with length

When the length of the cylinder is above 1,000 mm, the measurements at point 1 and point 2 agree well with the 2D model, with a slight difference attributed to FEA meshing. Below this length, the values diverge; however, the same qualitative behavior of the B-field (an induced outer dipole, an attenuated and rotated inner uniform field) still occurs. At point 3, the transverse magnitude and direction of the B-field shows only slight attenuation and phase lag, with the measured angle never varying more than 0.5 deg from the true angle (-90 deg, along the -Y axis). The most opportune place for a magnetometer on a rotating aluminum finite-length cylinder would therefore be directly above it. The steel case is shown in figure 18, where results are also compared to the infinite length 2D FEA model.

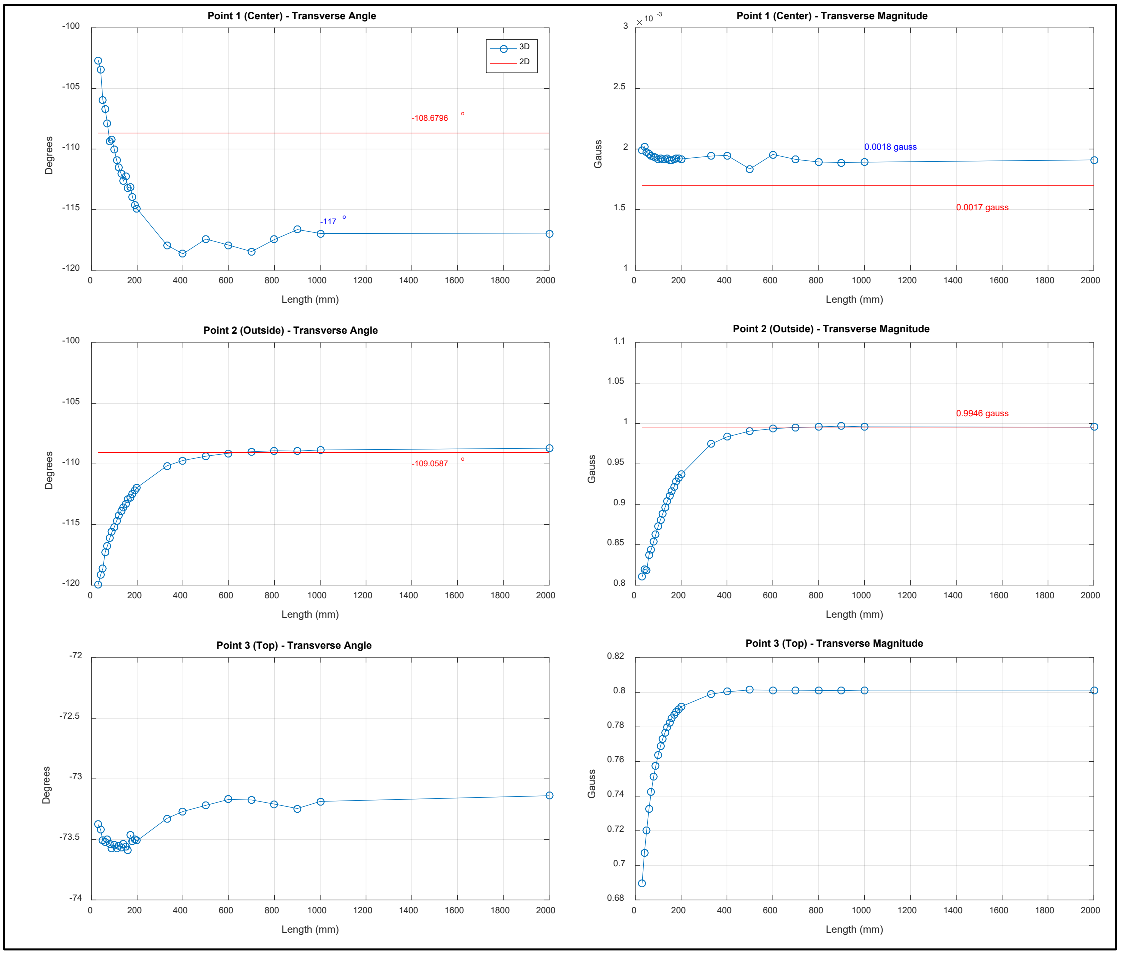

Figure 18
Steel cylinder varying with length

At point 1, there is a large discrepancy between the 2D and 3D models. This is attributed to a lack of adequate mesh resolution during modeling, which is a greater problem in the steel case than the aluminum case due to its smaller skin depth. At point 2, the 2D and 3D models agree well when the length of the cylinder is again above 1,000 mm. At point 3, the transverse magnitude and direction of the B-field shows larger attenuation and phase lag than in the aluminum case.

The B-field magnitude plots through cross sections of the aluminum and steel cylinder at the origin and at point 3, and streamlines of the B-field vector for the aluminum cylinder are shown in figures 19 through 23.

Length: 30 mm

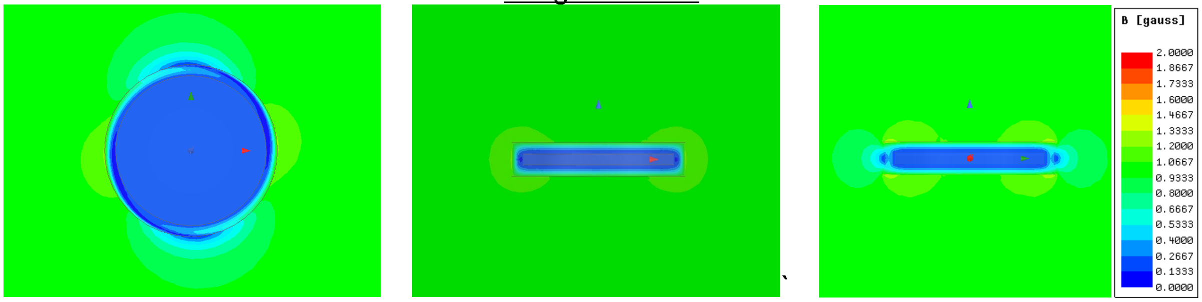

XY XZ YZ

Length: 130 mm

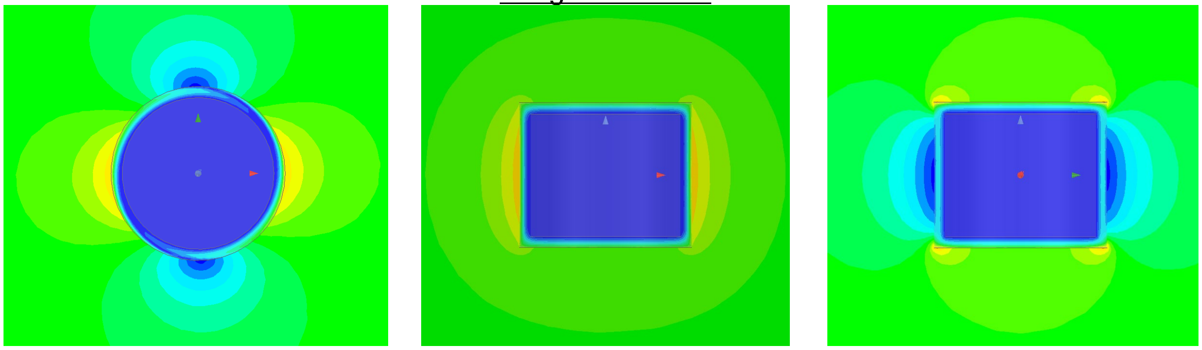

XY XZ YZ

Length: 330 mm

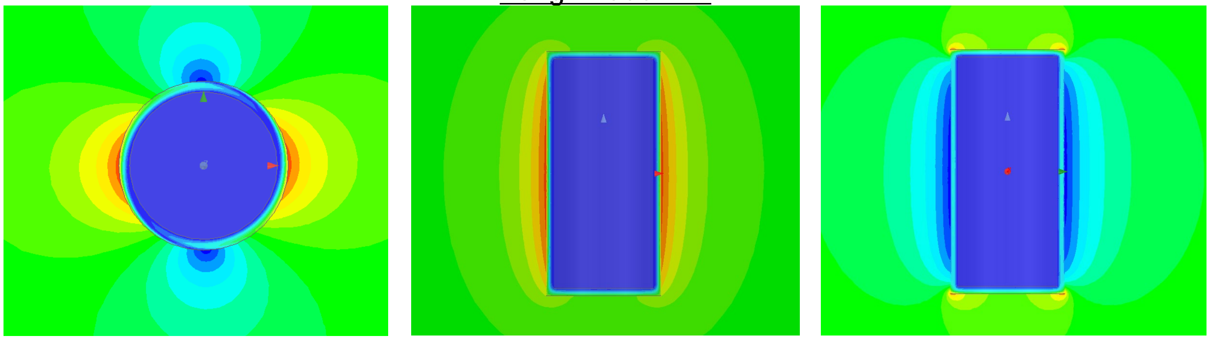

XY XZ YZ

Figure 19
B-field magnitude of finite-length aluminum cylinder within a rotating uniform field in the XY plane at 300 HZ

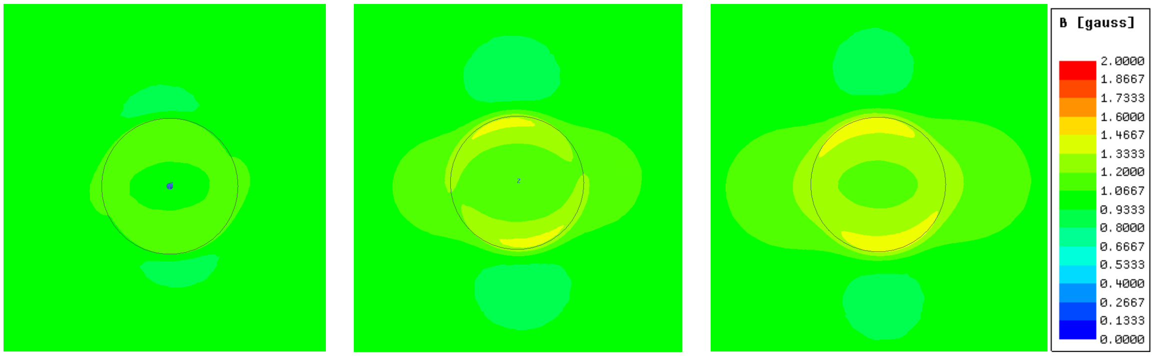

Length: 30 mm Length: 130 mm Length: 330 mm

Figure 20
B-field magnitude at point 3 top on the XY plane

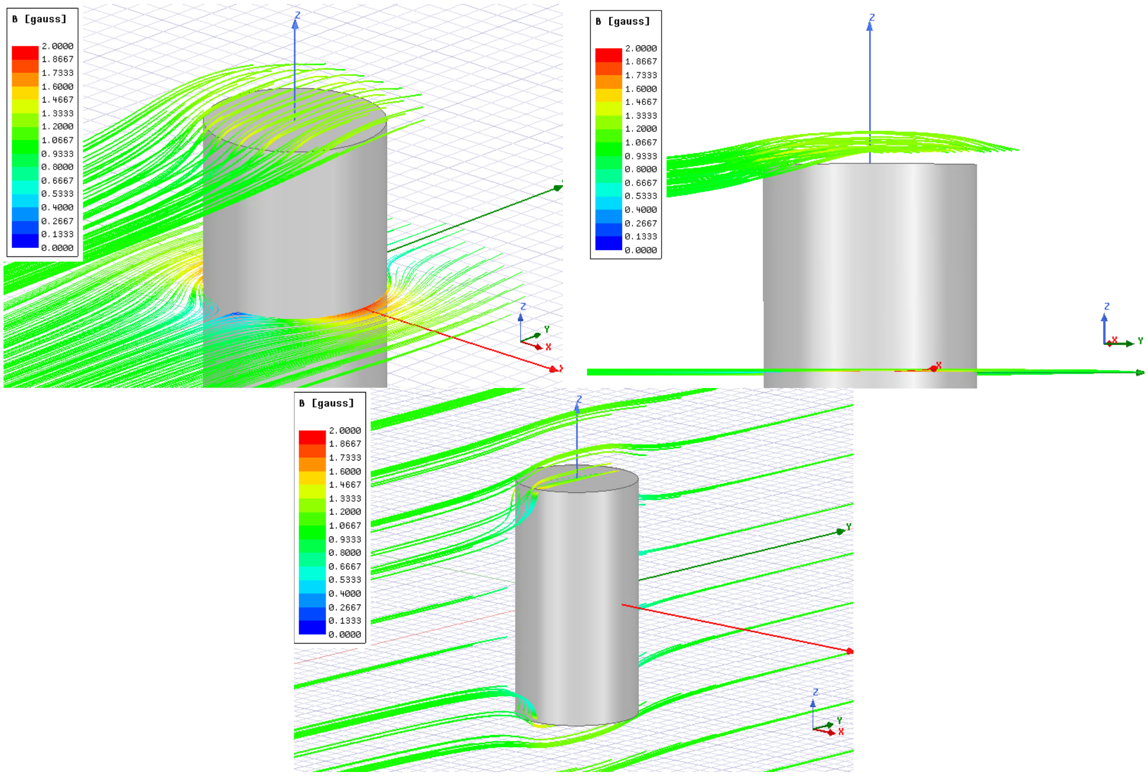

Figure 21
B-field vector streamlines of the aluminum cylinder, length 300 mm

Length: 30 mm

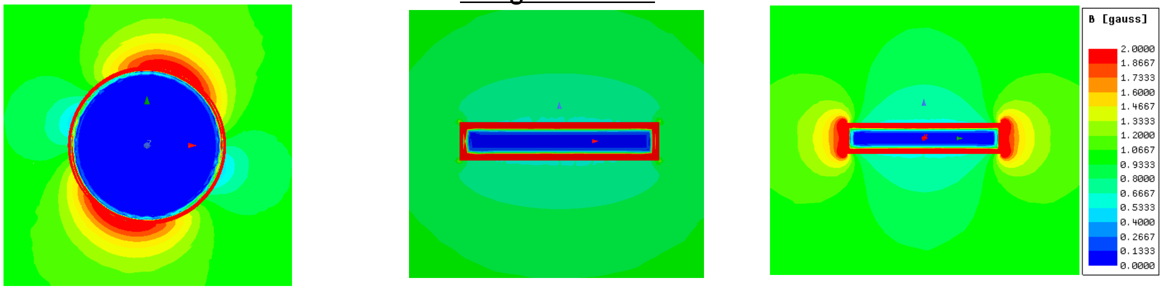

XY XZ YZ

Length: 130 mm

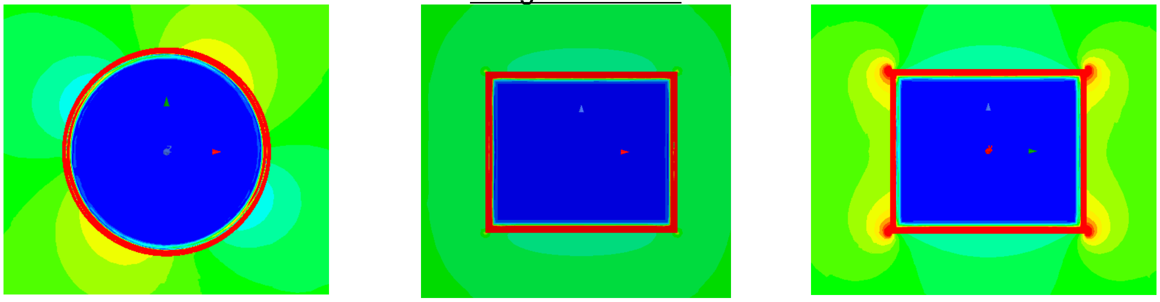

XY XZ YZ

Length: 330 mm

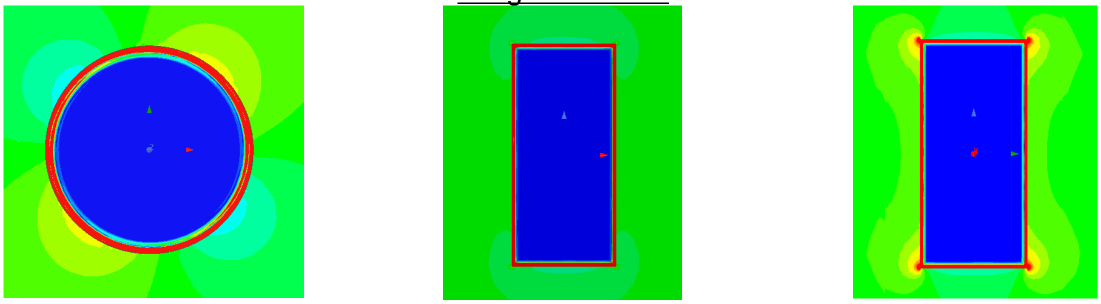

XY XZ YZ

Figure 22
B-field magnitude of finite-length closed steel cylinder subject to a rotating uniform field directed along XY plane at 300 HZ, at phase 0

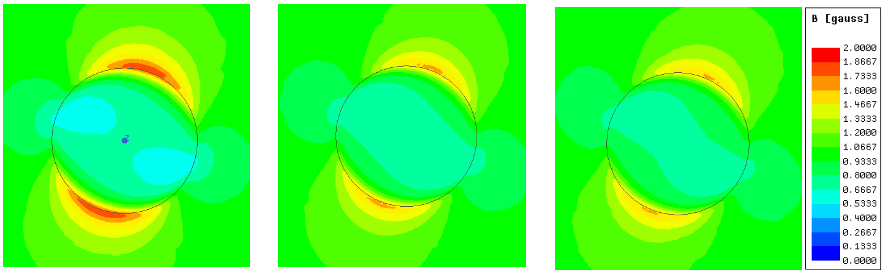

Length: 30mm Length: 130mm Length: 330mm

Figure 23
3D B-field magnitude at point 3 top along the XY plane

Streamlines of the B-field vector field outside the cylinders are shown in figures 24 and 25. These were solved by using aluminum and steel impedance boundary condition on the cylinder’s outer surface instead of meshing the conducting region and cylinder interior. This greatly reduces simulation time at the expense of slight inaccuracy in field magnitudes directly near the cylinder’s surface and only solving for the B-field outside the cylinder.

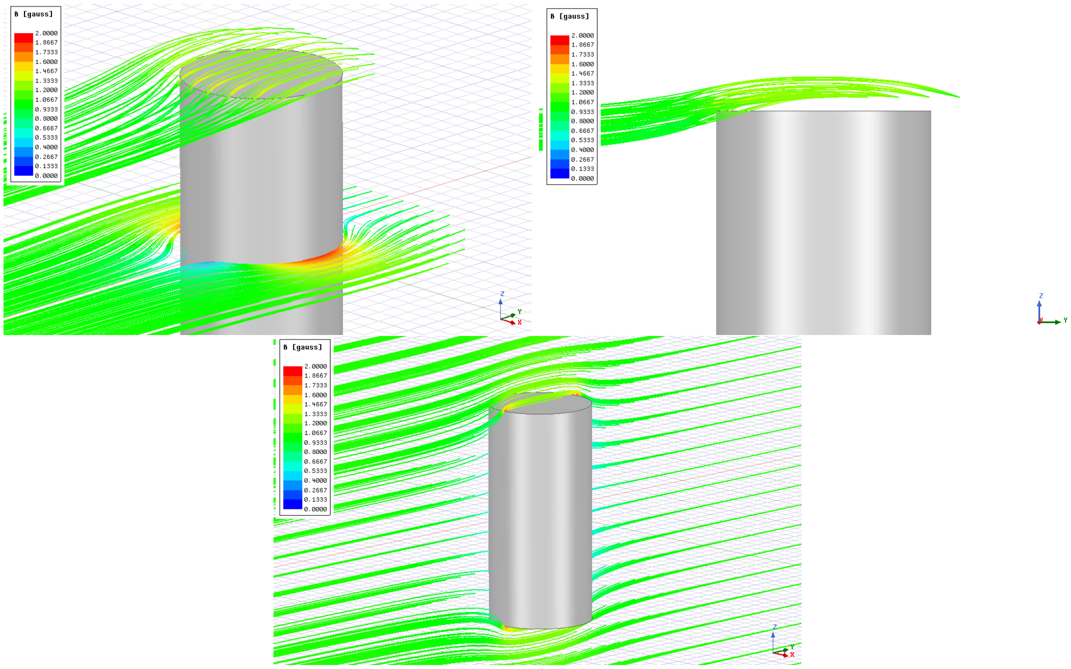

Figure 24
B-field vector streamlines of the aluminum cylinder, length 330 mm

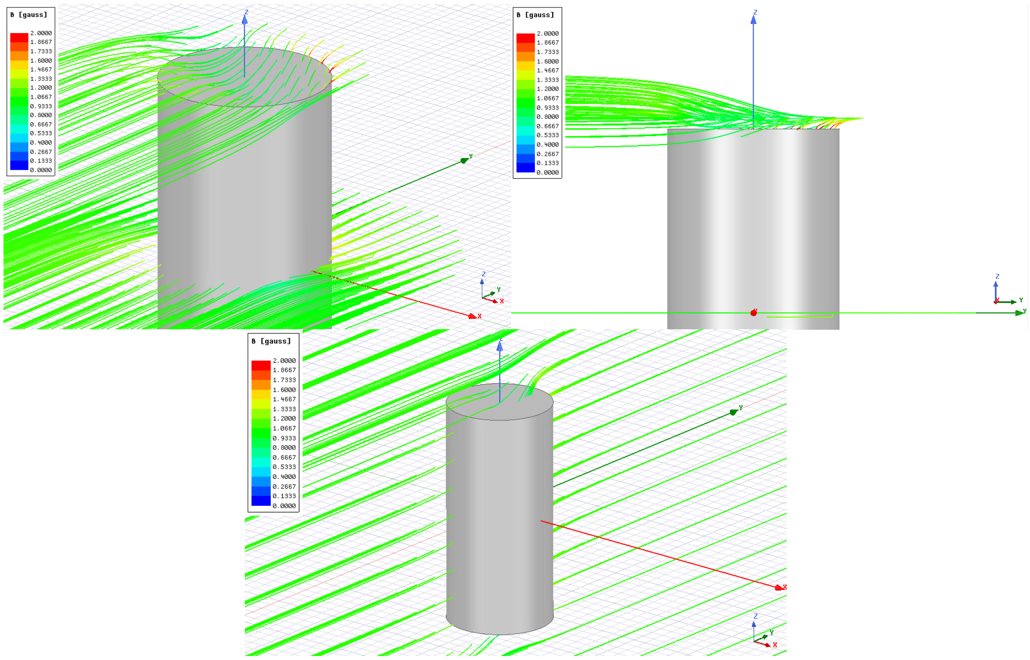

Figure 25
B-field vector streamlines of the steel cylinder, length 330 mm

OPTIMUM PLACEMENT OF MAGNETOMETERS

For accurate roll-angle measurements, the optimum placement of a magnetometer on a thick-walled projectile, when it must be placed midway on the projectile body so that thick shell model is valid, is outside the cylinder rather than inside. Despite both regions suffering from eddy-current distortions, the outer region suffers less. The magnitude and phase variation of the induced outer dipole is over 200 to 300 Hz (the typical range of roll rates of a spin-stabilized artillery projectile in flight) and also over tactical operating temperatures. This is significantly less than the magnitude and phase variation occurring with the interior field.

Additionally, if the magnetometer could be practically placed outside the shell, best-fit ellipse routines could be used to estimate the outer dipole formed and recover the true roll angle. The projectile could be allowed to rotate several times, with measurements captured by an on-board processor while estimating the best-fit ellipse and finding the major and minor axes. Once the processor has locked onto the ellipse, it would have an estimate of the true roll angle relative to the geomagnetic field, valid for at least the next several cycles when neither the spin rate nor the temperature of the shell change greatly. This method is not available for a magnetometer placed inside the shell.

If the choice of material for a projectile is available, it is apparent that using non-ferrous material (such as aluminum) would help the situation. As the projectile de-spins during flight, the angle of the outer dipole moment will change only slightly. This is not the case if the shell material has a high relative permeability, such as with steel.

Finally, for a finite-length aluminum cylinder, the optimum placement of a magnetometer is above it, where the roll angle determined from the transverse axes will undergo only a minute offset from eddy-current distortion.

CONCLUSIONS

A projectile body was modelled as a hollow infinite cylinder in order to study the effects of distortion on the transverse component of geomagnetic field as the projectile spins during flight. A thick shell model was derived, which captures the effects of magnetic polarization of the material as well as magnetic diffusion through the sidewalls of the projectile. The model shows that an induced magnetic dipole moment is formed on the exterior of the cylinder, with a magnitude and phase that vary with roll rate and material temperature, and which acts to spoil roll angle measurements for a magnetometer placed outside the shell. These could possibly be corrected using best-fit ellipse routines. A uniform field is formed on the interior of the cylinder, with a magnitude and phase angle that is attenuated and shifted relative to the original field. The attenuation and shifting factor vary with changes in spin rate, with the material properties of the shell and with the material temperature. An exploration of finite-length cylinder was also performed, which agreed with the infinite cylinder thick shell model at the mid-plane as the length increased.

REFERENCES

1. Harkins, T., "On the Viability of Magnetometer-Based Projectile Orientation Measurements," Technical Report ARL-TR-4310, U.S. Army Research Laboratory, Aberdeen Proving Ground, MD, November 2007.

2. Harkins, W., "Measuring In-Flight Angular Motion With a Low-Cost Magnetometer," Technical Report ARL-TR-4244, U.S. Army Research Laboratory, Aberdeen Proving Ground, MD, September 2007.

3. Wilson, M., Projectile Navigation and the Application to Magnetometers, University of Delaware, Newark, DE, 2007.

4. Rogers, J., Costello, M., Harkins, T., and Hamaoui, M., "Effective Use of Magnetometer Feedback for Smart Projectile Applications," Navigation, Vol. 58, No. 10, September 2011.

5. Knoepfel, H. E., Magnetic Fields: A Comprehensive Theoretical Treatise for Practical Use, John Wiley & Sons, Inc., Hoboken, NJ, 2000.

6. Olver, F. W. J., Olde Daalhuis, A. B., Lozier, D. W., Schneider, B. I., Boisvert, R. F., Clark, C. W., Miller, B. R., and Saunders, B. V., eds., NIST Digital Library of Mathematical Functions. http://dlmf.nist.gov/, Release 1.0.18 of 2018-03-27.

APPENDIX A
THIN SHELL MODEL

The thin shell model treats the projectile body as a thin-walled cylindrical conducting shell of radius b, subject to a uniform transverse B-field oscillating in the Y-axis. As the thin shell wall has no volume, the model does not include the effects of material permeability.

One solution for this kind of problem can be found in [Haus]. There, the field surrounding the shell is solved with a B-field ansatz, and corresponding field boundary conditions. Here, the fields will be solved by utilizing the magnetic vector potential $\vec{A}$, and its corresponding boundary conditions.

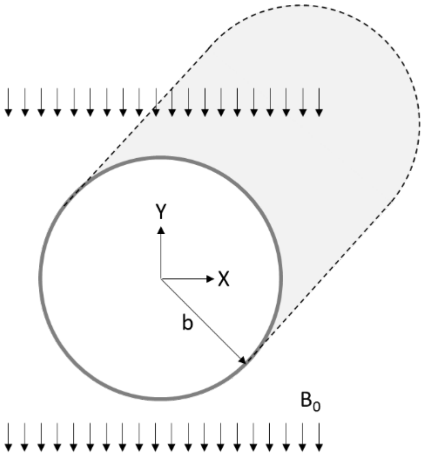

Figure A-1
Thin shell model

The magnetic vector potential inside and outside the shell is governed by the vector Laplace's equation. Assuming that the current around the shell is in the z-direction, only A_z is non-zero, which can be treated as a scalar field (akin to a magnetic scalar potential) which follows the scalar Laplace's equation. This equation in polar coordinates (r, ϕ) is

$$\text{(A.1)} \quad \nabla^2 A_z = 0$$

$$\text{(A.2)} \quad \frac{1}{r}\frac{d}{dr}\left(r\frac{dA_z}{dr}\right) + \frac{1}{r^2}\frac{d^2A_z}{d\theta^2} = 0$$

Far from the cylinder, we assume the potential takes the form of

$$\text{(A.3)} \quad A_z(r = \infty) = B_o \mathrm{r} \cos(\phi)\, e^{j\omega t}$$

This is the outer boundary condition for the vector potential for a uniform oscillating transverse B-field along the Y-axis, initially pointing in the -Y direction, and the first boundary condition of this solution. It satisfies the definition of magnetic vector potential

$$\text{(A.4)} \quad \vec{B} = \nabla x \vec{A}$$

Where

$$\text{(A.5)} \quad \vec{B} = -B_o \sin(\phi)\, e^{j\omega t}\hat{r} - B_o \cos(\phi) e^{j\omega t}\hat{\phi}$$

Separation of variables can be used to solve for the vector potential, we assume that A_z is a product solution of the form:

$$\text{(A.6)} \quad A_z = R(r)\theta(\phi)T(t)$$

$$\text{(A.7)} \quad T(t) = e^{j\omega t}$$

The general solution to Laplace's equation can be found in Chapter 5 of [Haus], where we can deduce that the separation constant is non-zero. Collecting the terms of the general solution, and comparing to the outer boundary condition, only those terms proportional to cos(φ) and sin (φ) are non-zero. We are left only with

$$\text{(A.8)} \quad A_{out} = \left(B_o r + \frac{C}{r}\right)\cos(\phi)\, e^{j\omega t}$$

$$\text{(A.9)} \quad A_{in} = \left(Dr\cos(\phi) + E\frac{1}{r}\cos(\phi) + Fr\sin(\phi) + G\frac{1}{r}\sin(\phi)\right) e^{j\omega t}$$

Which are the equations for the magnitude of A_z both outside and inside the shell. The 'z' subscript has been dropped for clarity. Terms proportional to r represent uniform B-fields, and terms proportional to $\frac{1}{r}$ represent B-fields due to dipoles. C,D,E,F,G represent unknown coefficients. Realizing that the potential must be exist at r=0 forces E=0 and G= 0. C represents the magnitude coefficient of an induced dipole outside the shell. D represents the magnitude of uniform field within the shell.
The magnetic vector potential is continuous over a boundary. Therefore at r=b, we can say that

$$\text{(A.10)} \quad A_{in}|_{r=b} = A_{out}|_{r=b}$$

Where the vector potential must be continuous across the shell. This is the second boundary condition of this solution. Solving at the boundary r=b and substituting the general solutions of A_{in} and A_{out} into the above yields F= 0 and solves for the remaining coefficient D in terms of B_o, b, and C:

$$\text{(A.11)} \quad \boxed{A_{out} = \left(B_o r + \frac{C}{r}\right)\cos(\phi)\, e^{j\omega t}}$$

$$\text{(A.12)} \quad \boxed{A_{in} = \left(B_o + \frac{C}{b^2}\right) r\cos(\phi)\, e^{j\omega t}}$$

The above equations show that the B-field outside the shell will be the sum of a uniform field and a dipole field (from the terms proportional to r and $\frac{1}{r}$), and inside the shell will be a single uniform field (from the two terms proportional to r).

The third boundary condition of this solution comes from Faraday's law applied to the magnetic vector potential. As outlined in Chapter 10.4 of [Haus], Faraday's law is the vector equation

$$\text{(A.13)} \quad \nabla x\vec{E} = -\frac{d\vec{B}}{dt}$$

Ohm's law provides a relation between the axial E-field and the axial current density J in the shell.

$$\text{(A.14)} \quad J_z = \sigma E_z$$

The thin shell model assumes that this current density is uniformly distributed between the thin cross section of the shell. Multiplying by the thickness of the shell, we can then create an equivalent axial surface current K_z:

$$\text{(A.15)}\quad K_z = \Delta J_z = \Delta\sigma E_z$$

Ampere's continuity condition relates the tangential fields on both sides of the shell to the axial surface current K_z.

$$\text{(A.16)}\quad K_z|_{r=b} = \left(H_\phi^{out} - H_\phi^{in}\right)\Big|_{r=b}$$

Which can be related to the axial E-field by

$$\text{(A.17)}\quad \Delta\sigma E_z|_{r=b} = \left(H_\phi^{out} - H_\phi^{in}\right)\Big|_{r=b}$$

In the Coulomb gauge, and assuming no active sources or free charge that create a non-zero electric scalar potential, the electric field is related to the magnetic vector potential by

$$\text{(A.18)}\quad \vec{E} = -\frac{d\vec{A}}{dt}$$

The above two equations can be combined to form

$$\text{(A.19)}\quad -\Delta\sigma \frac{dA_z}{dt}\bigg|_{r=b} = \left(H_\phi^{out} - H_\phi^{in}\right)\Big|_{r=b}$$

Then multiplied by the permeability of free space to yield

$$\text{(A.20)}\quad -\mu_0\Delta\sigma \frac{dA_z}{dt}\bigg|_{r=b} = \left(B_\phi^{out} - B_\phi^{in}\right)\Big|_{r=b}$$

Realizing that only A_z is non-zero, from $\vec{B} = \nabla \times \vec{A}$ we can therefore write

$$\text{(A.21)}\quad B_\phi = -\frac{dA_z}{dr}$$

Which can be used to substitute the B-field terms for A-field terms, yielding

$$\text{(A.22)}\quad -\mu_o\Delta\sigma \frac{dA}{dt}\bigg|_{r=b} = \left(-\frac{dA_{out}}{dr} - -\frac{dA_{in}}{dr}\right)\bigg|_{r=b}$$

Where the z-subscript has been dropped for clarity. This is used to solve for the induced dipole coefficient C. Substituting the general solutions for A_{in} and A_{out} into the right hand side, and differentiating with respect to r, then evaluating at $r = b$ yields:

$$\text{(A.23)}\quad -\mu_o\Delta\sigma \frac{dA}{dt}\bigg|_{r=b} = -\left(B_o - \frac{C}{b^2}\right)\cos(\phi)\, e^{j\omega t} + \left(B_o + \frac{C}{b^2}\right)\cos(\phi)\, e^{j\omega t}$$

Substituting into the left-hand side for A the general solution for A_{in} (which is permissible as A_{in} = A_{out} at that boundary), differentiating with respect to time, and evaluating at $r = b$ yields

$$\text{(A.24)}\quad \mu_o\Delta\sigma\left(B_o + \frac{C}{b^2}\right) b\cos(\phi)\, jw e^{j\omega t} = \left(B_o - \frac{C}{b^2}\right)\cos(\phi)\, e^{j\omega t} - \left(B_o + \frac{C}{b^2}\right)\cos(\phi)\, e^{j\omega t}$$

Removing the dependence on $\cos(\phi)\, e^{j\omega t}$yields

$$\text{(A.25)}\quad j\omega\mu_o\Delta\sigma\left(B_o+\frac{C}{b^2}\right)b=\left(B_o-\frac{C}{b^2}\right)-\left(B_o+\frac{C}{b^2}\right)$$

Solving for C yields

$$\text{(A.26)}\quad \boxed{C=\frac{-b^3 j\delta}{2+j\delta b}B_o}$$

Where δ is given by

$$\text{(A.27)}\quad \boxed{\delta=\mu_0\omega\sigma\Delta}$$

Utilizing the boxed equations, and the definition of $\vec{B}=\nabla x\vec{A}$ in polar coordinates

$$\text{(A.28)}\quad \vec{B}=\frac{1}{r}\frac{dA}{d\phi}\hat{r}-\frac{dA}{dr}\hat{\phi}$$

Yields solutions for the B-field inside and outside the cylinder.

$$\text{(A.29)}\quad \boxed{\vec{B}_{out}=-\left(B_o+\frac{C}{r^2}\right)\sin(\phi)\, e^{j\omega t}\hat{r}+\left(-B_o+\frac{C}{r^2}\right)\cos(\phi)\, e^{j\omega t}\hat{\phi}}$$

$$\text{(A.30)}\quad \boxed{\vec{B}_{in}=-\left(B_o+\frac{C}{b^2}\right)\sin(\phi)e^{j\omega t}\,\hat{r}-\left(B_o+\frac{C}{b^2}\right)\cos(\phi)\, e^{j\omega t}\hat{\phi}}$$

The constant C is proportional to the magnitude of the induced dipole outside the shell and the induced uniform B-field inside the shell. As the oscillating frequency of the outer uniform B-field becomes large:

$$\text{(A.31)}\quad C\ \rightarrow -b^2B_o$$

$$\text{(A.32)}\quad A_{out}=B_o\left(r-\frac{b^2}{r}\right)\cos(\phi)\, e^{j\omega t}$$

$$\text{(A.33)}\quad A_{in}=\left(B_o+\frac{-b^2B_o}{b^2}\right)r\cos(\phi)\, e^{j\omega t}=0$$

$$\text{(A.34)}\quad \vec{B}_{out}=-B_o\left(1-\frac{b^2}{r^2}\right)\sin(\phi)\, e^{j\omega t}\hat{r}-B_o\left(1-\frac{b^2}{r^2}\right)\cos(\phi)\, e^{j\omega t}\hat{\phi}$$

$$\text{(A.35)}\quad \vec{B}_{in}=0$$

The above equations indicate that the field outside the shell is the superposition of the original oscillating transverse B-field, and an induced two-dimensional dipole. The dipole is in-phase with the transverse field, and is of equal and opposite magnitude of the original imposed uniform field at, so as to completely divert magnetic flux around the shell. The B-field magnitude inside the shell is zero – the geomagnetic field has been bucked out of the cylinder completely. This is also the case where the thin shell is perfectly conducting.

It is the magnitude and phase variation of the complex variable C over frequency that causes the induced outer dipole and the field within the shell to vary with changes in ω. In the case where the thin shell is subject to a transverse rotating B-field, instead of a single oscillating transverse B-field (see appendix D), the phase variation of C will cause an angular offset between the axis of the dipole, the axis of the inner-field, and the rotating field.

Solving for the phase of C yields a very simple relation

$$\text{(A.36)} \quad \angle C = \arctan(\frac{2}{b\delta})$$

This shows that as the frequency of the oscillation increases, the induced outer dipole and the field within the shell become more geometrically aligned with the rotating outer transverse B-field.

The normalized magnitude, and phase angle for the induced outer dipole on a rotating, 1mm thick, 155mm diameter (77.5 mm radius), Aluminum shell of conductivity 3.5e7 S/m), from 0.1Hz to 1000Hz is plotted below. The magnitude is normalized to $-b^2 B_o$.

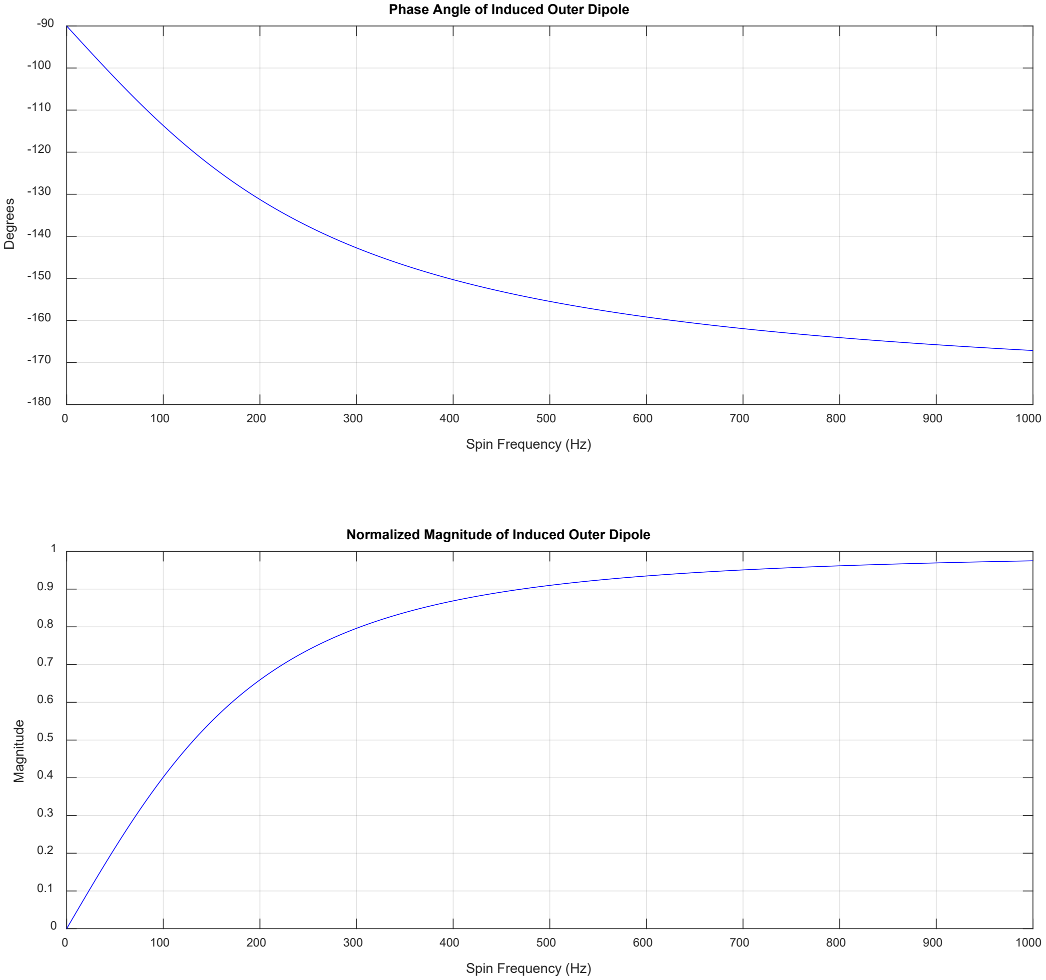

Figure A-2
Outer Induced Dipole Characteristics over Spin Frequency.

The normalized magnitude, and phase angle for the B-field in the interior of the shell is plotted below. The magnitude is normalized to B_o.

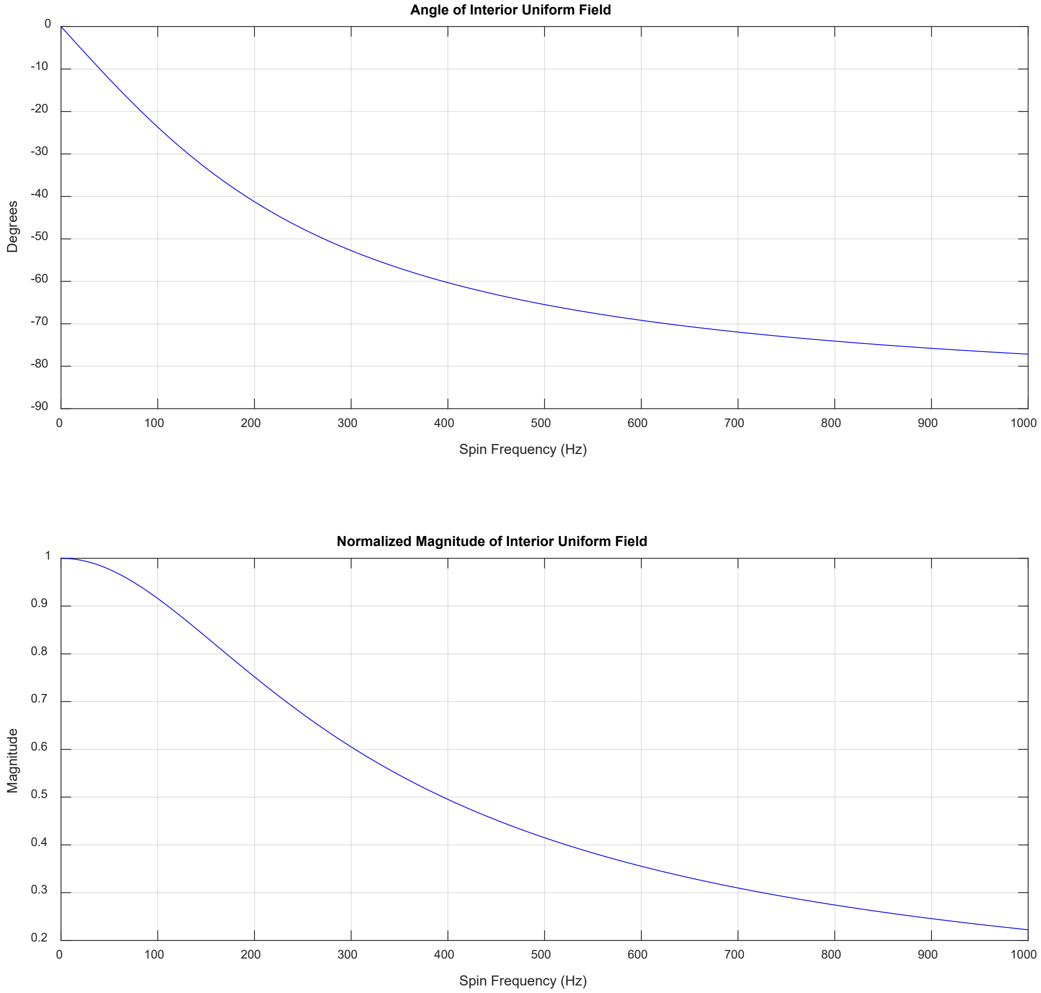

Figure A-3
Interior Uniform Field Characteristics over spin frequency

APPENDIX B
DERIVATION OF THE DIFFUSION EQUATION FOR THE MAGNETIC VECTOR POTENTIAL

Maxwell's equations, Ohm's law, and the charge conservation equation are as follows

$$\text{(B.1)} \quad \nabla \cdot \vec{E} = \frac{\rho_e}{\epsilon}$$

$$\text{(B.2)} \quad \nabla \times \vec{E} = -\frac{d\vec{B}}{dt}$$

$$\text{(B.3)} \quad \nabla \cdot \vec{B} = 0$$

$$\text{(B.4)} \quad \nabla \times \vec{B} = \mu \vec{J} + \mu\epsilon \frac{d\vec{E}}{dt}$$

$$\text{(B.5)} \quad \vec{J} = \sigma \vec{E}$$

$$\text{(B.6)} \quad \nabla \cdot \vec{J} + \epsilon \frac{d\rho_e}{dt} = 0$$

Where μ, ϵ, σ are the permeability, permittivity, and conductivity of the material. These are treated as constant and isotropic. In a magneto-quasi-static (MQS) system, the terms $\mu\epsilon \frac{d\vec{E}}{dt}$ and $\epsilon \frac{d\rho_e}{dt}$ are treated as negligibly, and are zero. With no free charge assumed, then ρ_e is also zero. The equations become

$$\text{(B.7)} \quad \nabla \cdot \vec{E} = \nabla \cdot \vec{J} = 0$$

$$\text{(B.8)} \quad \nabla \times \vec{E} = -\frac{d\vec{B}}{dt}$$

$$\text{(B.9)} \quad \nabla \cdot \vec{B} = 0$$

$$\text{(B.10)} \quad \nabla \times \vec{B} = \mu \vec{J}$$

$$\text{(B.11)} \quad \vec{J} = \sigma \vec{E}$$

Substituting:

$$\text{(B.12)} \quad \nabla \times \vec{B} = \mu\sigma \vec{E}$$

And defining the magnetic vector potential $\vec{A}$

$$\text{(B.13)} \quad \vec{B} = \nabla \times \vec{A}$$

We have

$$\text{(B.14)} \quad \nabla \times \nabla \times \vec{A} = \mu\sigma \vec{E}$$

The double-curl vector identity is as follows

$$\text{(B.15)} \quad \nabla \times \nabla \times \vec{A} = \nabla(\nabla \cdot \vec{A}) - \nabla^2 \vec{A}$$

Which gives

$$\text{(B.16)} \quad \nabla(\nabla \cdot \vec{A}) - \nabla^2 \vec{A} = \mu\sigma \vec{E}$$

From the E-field curl equation, we can define

$$\text{(B.17)}\quad \nabla \times \left(\vec{E} + \frac{d\vec{A}}{dt}\right) = 0$$

The term in the parenthesis can be treated as the gradient of scalar function, usually referred to as the electric scalar potential Φ

$$\text{(B.18)}\quad -\nabla\Phi = \vec{E} + \frac{d\vec{A}}{dt}$$

Which we can then solve for E and use to define

$$\text{(B.19)}\quad \nabla\left(\nabla \cdot \vec{A}\right) - \nabla^2\vec{A} = -\mu\sigma\nabla\Phi - \mu\sigma\frac{d\vec{A}}{dt}$$

At this point, we can do one of two things. Because of the gauge invariance of A, we can create the following gauge:

$$\text{(B.20)}\quad \nabla \cdot \vec{A} = -\mu\sigma\Phi$$

Which cancels from the equation and yields the diffusion equation for A

$$\text{(B.21)}\quad \nabla^2\vec{A} = \mu\sigma\frac{d\vec{A}}{dt}$$

Alternatively, as per [Knoepfel] Chapter 4, we can work in the Coulomb gauge.

$$\text{(B.22)}\quad \nabla \cdot \vec{A} = 0$$

Taking the dot product of the electrical scalar potential equation

$$\text{(B.23)}\quad -\nabla \cdot \nabla\Phi = \nabla \cdot \vec{E} + \frac{d(\nabla\cdot\vec{A})}{dt}$$

$$\text{(B.24)}\quad \nabla^2\Phi = 0$$

We assume that Φ is the electric scalar potential created by active sources and free charge, which will not exist in either the thin or thick shell models of this report, yielding

$$\text{(B.25)}\quad \nabla\Phi = 0$$

Which yields the same diffusion equation for A once more.

$$\text{(B.26)}\quad \nabla^2\vec{A} = \mu\sigma\frac{d\vec{A}}{dt}$$

APPENDIX C
GENERAL SOLUTION TO THE DIFFUSION EQUATION IN POLAR COORDINATES

$$\text{(C.1)} \quad \nabla^2 \vec{A} = \mu\sigma \frac{d\vec{A}}{dt}$$

is a vector diffusion equation. In both the thin shell and thick shell models, only A_z is non-zero, and the equation becomes the scalar diffusion equation in polar coordinates:

$$\text{(C.2)} \quad \frac{1}{r}\frac{d}{dr}\left(r\frac{dA_z}{dr}\right) + \frac{1}{r^2}\frac{d^2A_z}{d\theta^2} + \frac{d^2A_z}{dz^2} = \mu\sigma\frac{dA_z}{dt}$$

The term $\frac{d^2A_z}{dz^2}$ on the left-hand side is dropped, as A_z is uniform along the cylinder's z-axis. Finally, with the differentiation chain-rule applied to the multiplicand in the parenthesis, the equation becomes:

$$\text{(C.3)} \quad \frac{1}{r}\left(r\frac{d^2A_z}{dr^2} + \frac{dA_z}{dr}\right) + \frac{1}{r^2}\frac{d^2A_z}{d\theta^2} = \mu\sigma\frac{dA_z}{dt}$$

Distributing the $\frac{1}{r}$ factor yields the equation below, where the left-hand side consists of three terms in ascending powers of $\frac{1}{r}$:

$$\text{(C.4)} \quad \frac{d^2A_z}{dr^2} + \frac{1}{r}\frac{dA_z}{dr} + \frac{1}{r^2}\frac{d^2A_z}{d\theta^2} = \mu\sigma\frac{dA_z}{dt}$$

We assume that A_z is a product solution of the form:

$$\text{(C.5)} \quad A_z = R(r)\theta(\phi)T(t)$$

The equation becomes

$$\text{(C.6)} \quad R''\theta T + \frac{R'\theta T}{r} + \frac{R\theta''T}{r^2} = \mu\sigma R\theta T'$$

Where the prime superscript indicates differentiation with respect to each separated solution's independent variable. Multiplying throughout by r^2 yields

$$\text{(C.7)} \quad r^2R''\theta T + rR'\theta T + R\theta''T = \mu\sigma r^2 R\theta T'$$

Lastly by dividing by all terms by $R\theta T$ yields

$$\text{(C.8)} \quad \frac{r^2R''}{R} + \frac{rR'}{R} + \frac{\theta''}{\theta} = \mu\sigma r^2\frac{T'}{T}$$

We then assume a complex-exponential dependence for T, so that

$$\text{(C.9)} \quad T = e^{j\omega t}$$

Where substituting gives

$$\text{(C.10)} \quad \frac{r^2R''}{R} + \frac{rR'}{R} + \frac{\theta''}{\theta} = j\omega\mu\sigma r^2$$

And then rearranging so that functions of R and θ are on opposite sides:

$$\text{(C.11)} \quad \frac{r^2R''}{R} + \frac{rR'}{R} - j\omega\mu\sigma r^2 = -\frac{\theta''}{\theta}$$

The above equation is only true if both sides are equal to a constant. We introduce the separation constant υ^2

$$\text{(C.12)}\ \frac{r^2R''}{R}+\frac{rR'}{R}-j\omega\mu\sigma r^2=\upsilon^2$$

$$\text{(C.13)}\ -\frac{\theta''}{\theta}=\upsilon^2$$

Rearranging yields:

$$\text{(C.14)}\ r^2R''+rR'-(j\omega\mu\sigma r^2+\upsilon^2)R=0$$

$$\text{(C.15)}\ \theta''=-\upsilon^2\theta$$

By making the substitution

$$\text{(C.16)}\ \beta^2=j\omega\mu\sigma$$

$$\text{(C.17)}\ \alpha^2=(\beta r)^2$$

Gives the modified Bessel's equation[1] (ref. 6), and the harmonic equation respectively.

$$\text{(C.18)}\ r^2R''+rR'-(\alpha^2+\upsilon^2)R=0$$

$$\text{(C.19)}\ \theta''=-\upsilon^2\theta$$

Whose general solutions are

$$\text{(C.20)}\ R(r)=CI_\upsilon(\beta r)+DK_\upsilon(\beta r)$$

$$\text{(C.21)}\ \theta(\phi)=Acos(\upsilon\phi)+Bsin(\upsilon\phi)$$

Where A,B,C,D are unknown coefficients, and I_υ and K_υ are modified Bessel functions of the first and second kind of order υ, where υ must be an integer for $\theta(\phi+2\pi)=\theta(\phi)$. Modified Bessel functions are also used in [Smythe] (see Chapter 11). The positive root of α (e.g. βr and not $-\beta r$) is used as the arguments of the functions, which corresponds to inwardly moving diffusion towards the origin. The general solution for A_z becomes

$$\text{(C.22)}\ A_z=\sum_{\upsilon=-\infty}^{\infty}\big(Acos(\upsilon\phi)+Bsin(\upsilon\phi)\big)\big(CI_\upsilon(\beta r)+DK_\upsilon(\beta r)\big)\,e^{j\omega t}$$

---

[1] Choosing $T=e^{-j\omega t}$ would lead to the regular Bessel's equation and the associated Bessel functions as solutions.

APPENDIX D
ROTATING SCALAR FIELD AND VECTOR FIELDS

Define a rotating real scalar field in polar coordinates, as a function of $(r, \phi, \omega t)$ that satisfies the following:

$$\text{(D.1)} \quad R(r, \phi, \omega t + \theta_1) = R(r, \phi - (\omega t + \theta_1))$$

Consider a complex valued scalar field $F(r, \phi, \omega t)$ as a function of the following form:

$$\text{(D.2)} \quad F(r, \phi, \omega t) = R(r) C_m e^{j\angle C} \cos(\phi)\, e^{j\omega t}$$

Where R(r) is a real-valued function of r , $C = C_m e^{j\angle C}$ is a complex constant. Define the quadrature-phase shifted version as follows

$$\text{(D.3)} \quad F_q = F\left(r, \phi + \frac{\pi}{2}, \omega t + \frac{\pi}{2}\right)$$

The sum of F and F_q yield

$$\text{(D.4)} \quad F_{total} = F + F_q$$

$$\text{(D.5)} \quad F_{total} = R(r) C_m e^{j\angle C} \cos(\phi)\, e^{j\omega t} + R(r) C_m e^{j\angle C} \cos\left(\phi + \frac{\pi}{2}\right) e^{j(\omega t + \frac{\pi}{2})}$$

$$\text{(D.6)} \quad Re\{F_{total}\} = R(r) C_m \cos(\phi) \cos(\omega t + \angle C) + R(r) C_m \sin(\phi) \sin(\omega t + \angle C)$$

$$\text{(D.7)} \quad Re\{F_{total}\} = R(r) C_m \cos(\phi - (\omega t + \angle C))$$

Therefore $Re\{F_{total}\}$ is a rotating and real scalar field, whose values rotate counter-clockwise about the origin with time. The phase angle of C acts to tilt $Re\{F_{total}\}$ by an extra amount around the origin, while the magnitude C_m acts to scale the magnitude of $Re\{F_{total}\}$.
Define a rotating real vector field as follows

$$\text{(D.8)} \quad \vec{V}(r, \phi, \omega t + \theta_1) = \boldsymbol{R}(\omega t + \theta_1) \vec{V}(r, \phi)$$

$$\text{(D.9)} \quad \begin{bmatrix} V_r(r, \phi, \omega t) \\ V_\phi(r, \phi, \omega t) \end{bmatrix} = \begin{bmatrix} \cos(\omega t + \theta_1) & -\sin(\omega t + \theta_1) \\ \sin(\omega t + \theta_1) & \cos(\omega t + \theta_1) \end{bmatrix} \begin{bmatrix} V_r(r, \phi) \\ V_\phi(r, \phi) \end{bmatrix}$$

Where $\boldsymbol{R}(\omega t + \theta_1)$ is a rotation matrix around the origin. Consider V_r and V_ϕ that can be expressed in the following forms:

$$\text{(D.10)} \quad V_r(r, \phi, \omega t) = R(r) C_m e^{j\angle C} \sin(\phi)\, e^{j\omega t}$$

$$\text{(D.11)} \quad V_\phi(r, \phi, \omega t) = R(r) C_m e^{j\angle C} \cos(\phi)\, e^{j\omega t}$$

Define the quadrature-phase shifted versions as follows:

$$\text{(D.12)} \quad V_{qr}(r, \phi, \omega t) = V_r\left(r, \phi + \frac{\pi}{2}, \omega t + \frac{\pi}{2}\right)$$

$$\text{(D.13)} \quad V_{q\phi}(r, \phi, \omega t) = V_\phi\left(r, \phi + \frac{\pi}{2}, \omega t + \frac{\pi}{2}\right)$$

The sum of V_r and V_{qr} becomes

$$\overrightarrow{V_{tot}} = \left| \begin{matrix} R(r)C_m e^{j\angle C} \sin(\phi)\, e^{j\omega t} + R(r)C_m e^{j\angle C} \sin\left(\phi + \frac{\pi}{2}\right) e^{j(\omega t + \frac{\pi}{2})} \\ R(r)C_m e^{j\angle C} \cos(\phi)\, e^{j\omega t} + R(r)C_m e^{j\angle C} \cos\left(\phi + \frac{\pi}{2}\right) e^{j(\omega t + \frac{\pi}{2})} \end{matrix} \right| \tag{D.14}$$

Where

$$Re\{\overrightarrow{V_{tot}}\} = \left| \begin{matrix} R(r)C_m \sin(\phi) \cos(\omega t + \angle C) - R(r)C_m \cos(\phi) \sin(\omega t + \angle C) \\ R(r)C_m \cos(\phi) \cos(\omega t + \angle C) + R(r)C_m \sin(\phi) \sin(\omega t + \angle C) \end{matrix} \right| \tag{D.15}$$

$$Re\{\overrightarrow{V_{tot}}\} = \begin{bmatrix} \cos(\omega t + \angle C) & -\sin(\omega t + \angle C) \\ \sin(\omega t + \angle C) & \cos(\omega t + \angle C) \end{bmatrix} \begin{bmatrix} R(r)C_m \sin(\phi) \\ R(r)C_m \cos(\phi) \end{bmatrix} \tag{D.16}$$

Therefore $Re\{\overrightarrow{V_{tot}}\}$ is a rotating and real vector field, whose values rotates counter-clockwise about the origin in r, ϕ plane with time. The phase angle of C again acts to tilt $Re\{\overrightarrow{V_{tot}}\}$ by an extra amount around the origin, while the magnitude C_m acts to scale the magnitude of $Re\{\overrightarrow{V_{tot}}\}$.

BIBLIOGRAPHY

1. Hermann, H., James, M., Markus, Z., and Manuel, S., RES.6-001 “Electromagnetic Fields and Energy,” Spring 2008. Massachusetts Institute of Technology: MIT OpenCourseWare, https://ocw.mit.edu. License: Creative Commons BY-NC-SA.

2. Smythe, W. R., Static and Dynamic Electricity, McGraw-Hill, New York, NY, 1950.

3. Perry, M. and Jones, T., “Eddy Current Induction in a Solid Conducting Cylinder with a Transverse Magnetic Field,” IEEE Transactions on Magnetics, Vol. 14, No. 4, pp 227-232, July 1978.

4. Ziolkowski, M. and Gratkowski, S. R., “Shielding From External Magnetic Fields by Rotating Nonmagnetic Conducting Cylindrical Shells,” IEEE Transactions on Electromagnetic Compatibility, Vol. 51, No. 3, pp 720-724, August 2009.

5. Long, D. F., Lin, J., Zhang, X. M., and Li, J., “Orientation estimation algorithm applied to high-spin projectiles,” Measurement Science and Technology, Vol. 25, No. 6, June 2014.

DISTRIBUTION LIST

U.S. Army CCDC AC		
ATTN:	FCDD-ACE-K	
	FCDD-ACM-F,	D. Troast
	FCDD-ACM-AM,	M. Hollis
	FCDD-ACM-AA,	E. Marshall
	FCDD-ACM-FP,	C. Stout
	FCDD-ACM-FI,	C. Sandberg
	FCDD-ACW-WI,	R. Granitzki
	FCDD-ACM-FA,	T. Recchia
Picatinny Arsenal, NJ 07806-5000		

U.S. Army Research Laboratory		
ATTN:	DDRL-WML-F,	M. Hamaoui
	RDRL-SER-M,	S. Weiss
Aberdeen Proving Ground, MD 21005-5069		

Defense Technical Information Center (DTIC)
ATTN: Accessions Division
8725 John J. Kingman Road, Ste 0944
Fort Belvoir, VA 22060-6218

GIDEP Operations Center
P.O. Box 8000
Corona, CA 91718-8000
gidep@gidep.org

REVIEW AND APPROVAL OF ARDEC REPORTS

THIS IS A:

☒ **TECHNICAL REPORT** ☐ **SPECIAL REPORT**

☐ **MEMORANDUM REPORT** ☐ **ARMAMENT GRADUATE SCHOOL REPORT**

FUNDING SOURCE ARDEC S&T
[e.g., TEX3; 6.1 (ILIR, FTAS); 6.2; 6.3; PM funded EMD; PM funded Production/ESIP; Other (please identify)]

Infinite Cylinder Model for Magnetometers on Projectiles
Title
Project

Aaron Barton
Author/Project Engineer
Report number/Date received (to be completed by LCSD)

x3521
Extension
95
Building
RDAR-MEF-I
Author's Office Symbol

PART 1. **Must be signed before the report can be edited.**

a. The draft copy of this report has been reviewed for technical accuracy and is approved for editing.

b. Use Distribution Statement A ✓, B____, C____, D____, E____, or F____ for the reason checked on the continuation of this form. Reason: ____________

1. If Statement A is selected, the report will be released to the National Technical Information Service (NTIS) for sale to the general public. Only unclassified reports whose distribution is not limited or controlled in any way are released to NTIS.

2. If Statement B, C, D, E, or F is selected, the report will be released to the Defense Technical Information Center (DTIC) which will limit distribution according to the conditions indicated in the statement.

c. The distribution list for this report has been reviewed for accuracy and completeness.

Craig D. Sandberg 1 AUG 2018
Division Chief (Date)

PART 2. To be signed either when draft report is submitted or after review of reproduction copy.

This report is approved for publication.

Craig D. Sandberg 4 Aug 2020
Division Chief (Date)

8/20/18
RDAR-CIS (Date)

LCSD 49 (1 Sept 16)
Supersedes SMCAR Form 49, 20 Dec 06